DTIC FILE COPY.

②

REPORT DOCUMENTATION PAGE

AD-A222 853	**1b. RESTRICTIVE MARKINGS**
2b. DECLASSIFICATION / DOWNGRADING SCHEDULE	**3. DISTRIBUTION / AVAILABILITY OF REPORT** Approved for public release; distribution unlimited.

4. PERFORMING ORGANIZATION REPORT NUMBER(S) MDC QA052	**5. MONITORING ORGANIZATION REPORT NUMBER(S)** AFOSR.TR. 90-0547

6a. NAME OF PERFORMING ORGANIZATION McDonnell Douglas Research Laboratories	6b. OFFICE SYMBOL *(If applicable)*	7a. NAME OF MONITORING ORGANIZATION Same as 8a
6c. ADDRESS *(City, State, and ZIP Code)* McDonnell Douglas Corporation P.O. Box 516 St. Louis, MO 63166		**7b ADDRESS** *(City, State, and ZIP Code)* Same as 8c

8a. NAME OF FUNDING / SPONSORING ORGANIZATION Air Force Office of Scientific Research	8b. OFFICE SYMBOL *(If applicable)* NE	9. PROCUREMENT INSTRUMENT IDENTIFICATION NUMBER F49620-86-C-0108

8c. ADDRESS *(City, State, and ZIP Code)* Building 410 Bolling AFB, DC 20332-6448	10. SOURCE OF FUNDING NUMBERS			
	PROGRAM ELEMENT NO. 61102F	PROJECT NO. 2306	TASK NO. A1	WORK UNIT ACCESSION NO.

11 TITLE *(Include Security Classification)*

Growth and Deformation Mechanisms of Refractory Alloy Hybrid Materials

12. PERSONAL AUTHOR(S)

S. M. L. Sastry, D. S. Schwartz, D. M. Bowden, J. E. O'Neal

13a. TYPE OF REPORT Final Technical Report	13b. TIME COVERED FROM 9/86 TO 9/89	14. DATE OF REPORT *(Year, Month, Day)* 1989 April	15. PAGE COUNT 67

16. SUPPLEMENTARY NOTATION

17.	COSATI CODES		18. SUBJECT TERMS *(Continue on reverse if necessary and identify by block number)*
FIELD	GROUP	SUB-GROUP	titanium alloys, niobium alloys, hybrid materials, refractory
			materials, rapid solidification processing, oxide dispersions
			in-situ composites, whisker reinforcement, properties,

19. ABSTRACT *(Continue on reverse if necessary and identify by block number)*

Oxide-dispersion-strengthened and whisker/particulate reinforced titanium and niobium alloys produced by rapid solidification processing were investigated with the objectives of understanding the mechanisms of formation and growth of the secondary phases and how these factors determine strengthening mechanisms and thermal stability of Ti and Nb alloys. Nb alloys containing W, Hf, La, B, and C were prepared by nonconsumable electrode arc melting and microstructures were characterized. The alloys were rapidly solidified by electron beam melting and splat quenching and the rapidly solidified flakes were characterized by x-ray diffraction, optical metallography, and electron microscopy. The structure of RSP Ti alloys containing Al, Er, and B was examined in detail before and after heat treatment. Analytical transmission electron microscopy (ATEM) was used to determine dispersoid composition and dispersoid/matrix orientation relations. The detailed structure of two-phase $\alpha_2/\cdot$ lamellar colonies in Ti-36Al alloys was investigated by transmission electron microscopy (TEM). The mechanical properties of rapidly solidified alloys were determined by tensile testing of specimens prepared from

20. DISTRIBUTION / AVAILABILITY OF ABSTRACT ☐ UNCLASSIFIED/UNLIMITED ☒ SAME AS RPT ☐ DTIC USERS	21. ABSTRACT SECURITY CLASSIFICATION UNCLASSIFIED
22a NAME OF RESPONSIBLE INDIVIDUAL Rosenstein	**22b TELEPHONE** *(Include Area Code)* 202-767-4933	**22c OFFICE SYMBOL** NE

DD FORM 1473, 84 MAR

83 APR edition may be used until exhausted.
All other editions are obsolete

SECURITY CLASSIFICATION OF THIS PAGE

UNCLASSIFIED

90 05 25 103

18. continued

deformation mechanisms, growth kinetics, work hardening

19. continued

electron-beam-melted and splat-quenched flakes and extrusions prepared from plasma-arc-melted gas atomized powders. The effects on mechanical properties of size, shape, and morphology of reinforcements were determined.

PREFACE

This report was prepared by the McDonnell Douglas Research Laboratories (MDRL), St. Louis, MO, for the Air Force Office of Scientific Research, Washington, DC, under Contract F49620-86-C-0108. The AFOSR Program Manager was Dr. A. H. Rosenstein.

The work was performed in the Solid State Sciences Department of MDRL under the supervision of Dr. C. R. Whitsett. The principal investigator was Dr. S. M. L. Sastry, co-investigators were Dr. D. S. Schwartz, Dr. D. M. Bowden, and Mr. J. E. O'Neal.

This report has been reviewed and is approved.

C. R. Whitsett, Director-Research
McDonnell Douglas Research Laboratories

J. O. Dimmock, Staff Vice President, Research
McDonnell Douglas Research Laboratories

Accession For	
NTIS GRA&I	☒
DTIC TAB	☐
Unannounced	☐
Justification	
By	
Distribution/	
Availability Codes	
Dist	Avail and/or Special
A-1	

DTIC
COPY
INSPECTED
4

TABLE OF CONTENTS

LIST OF ILLUSTRATIONS

LIST OF TABLES

1. INTRODUCTION

A major challenge in the development of dispersion-hardened alloys is to produce a high volume-fraction of the fine hardening particles. This challenge has been met through the use of rapid solidification technology (RST). Application of RST to titanium alloys can produce oxide-dispersion-strengthened alloys having large volume-fractions of ≤ 100 (nm) incoherent oxide dispersoids, and in situ composites containing high-modulus whisker/ particulate reinforcements (References 1 and 2). These titanium alloys are a special class of refractory hybrid materials which have low density, yet have the high-temperature strength and stability required for use as hypersonic aircraft skins and structures.

Oxide dispersions in RST (Ti) alloys are produced by rapid solidification processing (RSP) and subsequent annealing of Ti/rare-earth alloys. Rapid solidification significantly increases the solid solubilities of rare-earth elements in Ti. Annealing causes the rare-earth elements to precipitate and scavenge interstitial oxygen from the Ti matrix, forming rare-earth oxide dispersoids.

Keywords: Titanium alloys, Niobium alloys, Hybrid materials, Refractory materials, Rapid Solidification Processing, Oxide dispersions,

RST in situ composites are so named because they contain large volume-fractions of reinforcing second-phase particles reminiscent of the filaments or whiskers used in metal-matrix composites. These reinforcing dispersoids are formed in situ in RST alloys either upon solidification or subsequently by controlled precipitation from the supersaturated solid solutions achievable only by RST. The physical conditions that govern the nucleation, growth, and matrix interactions of the reinforcing dispersoids in RST in situ composites are different from those that prevail in conventional alloys or metal-matrix composites.

The basic mechanisms by which oxide-dispersion-strengthened alloys and in situ composites are formed and imparted with stable high-temperature strength are not known quantitatively. The objective of the present investigation was to develop predictive models to describe the morphology and growth kinetics of the reinforcement phases and mechanical behavior of novel hybrid materials produced by RSP. Ti and Nb alloys containing large-aspect-ratio filamentary or equiaxed/spheroidal boride, carbide, and erbia

Composites, Whisker reinforcement, Properties

1

reinforcements were studied to determine the mechanisms of formation and growth of the secondary phases and to understand how these factors determine strengthening mechanisms and thermal stability.

2. ALLOY PREPARATION

2.1 Titanium Alloy Preparation

Titanium alloys with the nominal compositions shown in Table 1 were procured from Titanium Metals Corporation of America (TMCA). The alloys were selected to cover the technologically important matrix materials for titanium alloys: α-Ti, α_2 (Ti_3Al), and γ (TiAl). The alloying additions, erbium, boron, and carbon, were selected to produce both spherical and filamentary dispersoid morphologies. The erbium additions produced a spherical, incoherent oxide particle dispersion; the boron additions reacted with the titanium to form a dispersion of high-aspect-ratio titanium borides; the carbon additions reacted with the titanium matrix to form a dispersion of spherical titanium carbides.

Rapidly solidified alloys were produced with the objective of producing fine dispersions by controlling the degree of undercooling and cooling rates (Reference 3). Electron beam melting/splat quenching (EBSQ) and plasma arc melting/centrifugal atomization (PAMCA) techniques were used to produce Ti alloys containing a fine distribution of dispersoids.

2.1.1 Electron Beam Melting/Splat Quenching

Prealloyed ingots were prepared by nonconsumable electrode arc-melting in an argon atmosphere. Cylindrical specimens, 6 mm in diameter and 100 mm long, were prepared by electric discharge machining and used as feedstock for the EBSQ processing. A schematic of the EBSQ apparatus is shown in Figure 1. An electron beam is focused onto the end of a rotating rod of the desired alloy, where it melts the surface and produces a molten zone. The molten zone then forms drops which fall onto a rotating copper disk and are stretched into thin flakes under the combined actions of a high angular velocity and the centrifugal force of the rotating disk. Melt-drop size and drip rate are controlled by varying the angular velocity of the alloy rod, vertical traverse rate of the rod, and the intensity of the electron beam. Flake thickness is predominantly a function of the angular velocity of the Cu quenching disk. EBSQ has an estimated cooling rate of 1.5 - 50 $\times$ 10^5 K/s

Table 1. Compositions of titanium alloy powders.

Element	Concentration (wt%)					
	Alloy 1	Alloy 2	Alloy 3	Alloy 4	Alloy 5	Alloy 6
Al	0	0	17.0	16.8	34.6	35.6
B	0.91	0	1.03	0	1.01	0
Er	0	1.55	0	1.64	0	1.73
O	0.21	0.12	0.14	0.13	0.33	0.098
C	0.11	0.33	0.094	0.10	0.080	0.040
N	0.33	0.048	0.090	0.062	0.15	0.051
H	30 ppm	24 ppm	18 ppm	26 ppm	21 ppm	9 ppm
O + C	0.32	0.55	0.234	0.23	0.41	0.138

90-220-173b
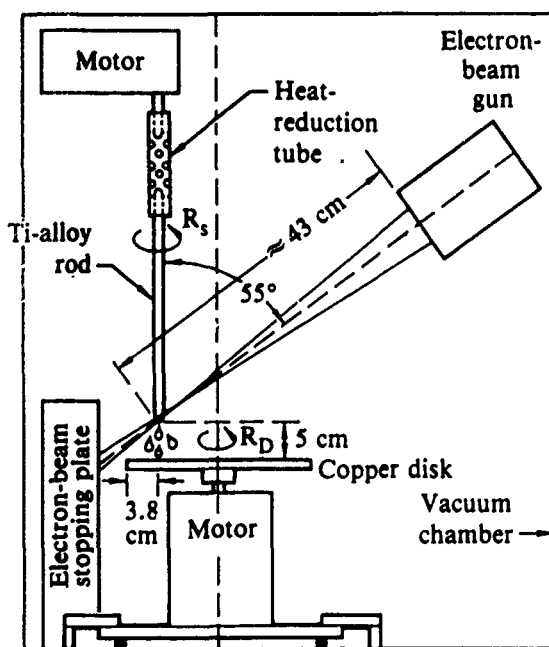
90-224-133

Figure 1. Schematic diagram of the electron-beam splat-quenching apparatus for the rapid solidification of titanium and niobium alloys.

for flake thicknesses of 50 - 100 μm (Reference 4). Typical flakes produced by this technique are shown in Figures 2a-2d.

2.1.2 Plasma Arc Melting/Centrifugal Atomization

Rapidly solidified powders were produced at MDRL using the PAMCA apparatus shown schematically in Figure 3. Ti-alloy ingots weighing roughly 9 kg were produced by plasma arc melting the constituent materials in a water-cooled copper hearth, which was sealed at the bottom by a graphite plug. The molten ingot was then allowed to solidify, removed from the hearth, inverted, remelted, and resolidified to ensure compositional homogeneity.

Prior to powder production, the starting ingot was inverted once more and the graphite plug was replaced with an induction-heated graphite tundish (Figure 3). The alloy ingot was then melted with 110- and 55-kW transfer plasma arc torches. The 110-kW melt torch was kept in motion over the melt to maintain melt-supply while the 55-kW tundish torch was positioned directly over the graphite tundish. As the ingot melted, the molten alloy flowed out of the hearth through a 30-kW induction-heated graphite tundish onto a 50-mm-diameter disk rotating at 20,000 rpm. The melt stream was subsequently atomized into fine droplets by the centrifugal force of the rotating disk. The melt-droplets then rapidly solidified into 30- to 600-μm-diameter powder particles by radiative and convective heat-loss to the helium cooling-gas flowing through the chamber. The powder particles were collected in a container at the bottom of the atomization chamber.

2.2 Rapid Solidification Processing of Niobium Alloys

Niobium alloys of compositions listed in Table 2 were procured from Teledyne Wah Chang, Albany, OR. Initial attempts to produce Nb-Er alloys were unsuccessful due to volatilization of the Er during melting. The rare earths Y and La were selected because of their high heats of vaporization, and ingots containing these elements were successfully produced. The La- and Y-containing alloys allow us to study growth of rare-earth dispersoids in various niobium solid-solution matrices. Since both W and Hf are common solid-solution-strengthening additions in commercial niobium alloys, they
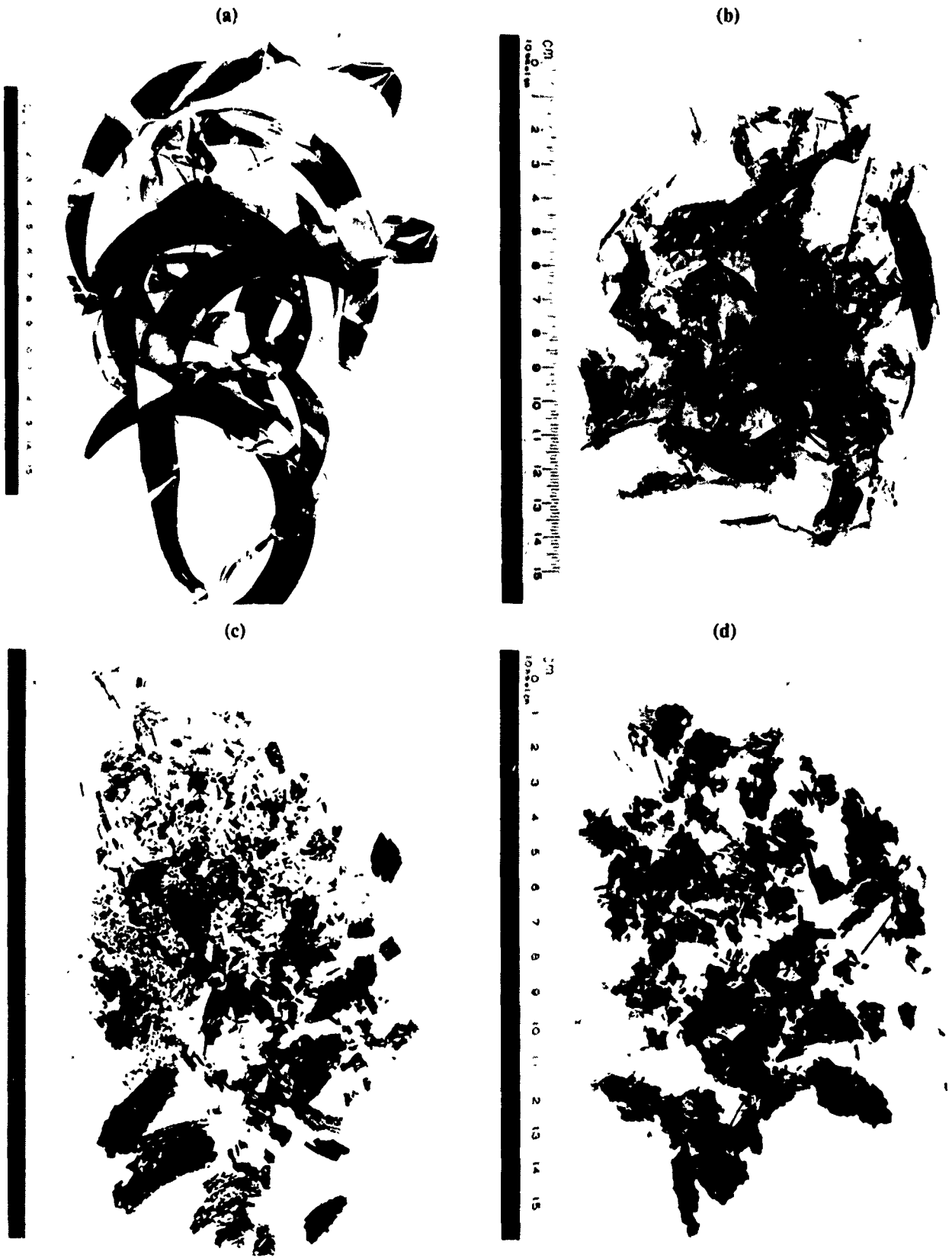
Figure 2. Rapidly solidified flakes of (a) Ti-2.0Er, (b) Ti-1.0B, (c) Ti-36Al-2Er, and (d) Ti-36Al-1.5B alloys produced by electron beam melting and splat quenching.

90-224-134

6
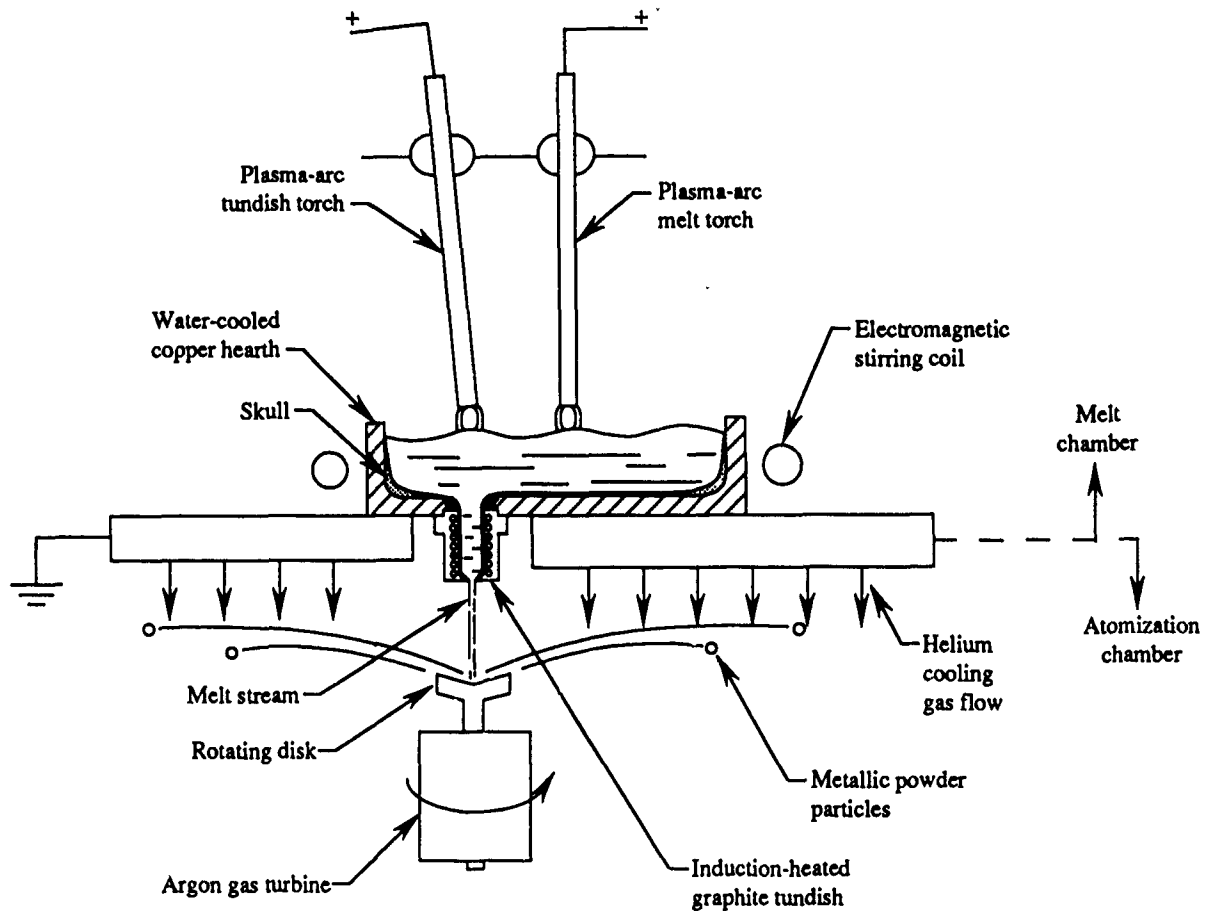
Figure 3.   Schematic of a plasma-arc-melting/centrifugal-atomization (PAMCA) apparatus.

90-224-135b

Table 2. Nominal compositions of niobium alloys.

Nb-2La
Nb-15Hf-2La
Nb-15W-2La
Nb-30Hf-2La
Nb-30W-2La
Nb-15Hf-1Y
Nb-15W-1Y
Nb-0.2C
Nb-6Zr-0.2C
Nb-30W-6Zr-0.2C

90-224-218

are valid choices for solute addition. Furthermore, W and Hf provide different levels of matrix lattice strain and influence diffusion (and thus growth kinetics) differently.

2.3 Alloy Characterization

The product alloys were given a range of heat treatments, and the resulting microstructures were examined by optical and electron microscopy. Tensile specimens were prepared from both EBSQ flakes and extrusions of powder produced by PAMCA, and tensile tests were performed at room and elevated temperatures. Quantitative size and shape analyses were performed on the dispersoids in the alloys and were related to the tensile data.

3. MICROSTRUCTURES OF RAPIDLY SOLIDIFIED ALLOYS

The microstructures of four alloys prepared by electron beam-melting and splat quenching (EBSQ) were examined in detail. The alloys investigated were Ti-1.25Er, Ti-1.5B, Ti-36Al-2.0Er, and Ti-36Al-1.5B. Samples of each of the four Ti alloys were annealed for 1 h at 800, 1000, and 1200°C. The EBSQ flakes were sealed in evacuated quartz tubes, annealed, and then quenched in water while still encapsulated. Microstructural analyses were performed by optical metallography, scanning electron microscopy (SEM), and transmission electron microscopy (TEM). Samples for TEM were prepared by electropolishing or ion milling, as required.

3.1 Microstructure of Ti-1.5B

In rapidly solidified Ti-1.5B, the boron additions dissolve in molten titanium and precipitate during solidification to produce elongated needles of the monoboride, TiB. The borides are clearly visible in the scanning electron micrograph in Figure 4. Typically, the borides are 0.1 - 1.0 μm long, with an aspect ratio of approximately 6:1. The borides are well dispersed throughout the matrix, with little dispersoid clustering or grain-boundary precipitation, as can be seen in the transmission electron micrograph in Figure 5. The needles tend to be aligned, with a definite orientation relationship to the matrix. The boride needles are approximately equiaxed hexagonal in cross section.

Annealing the sample at 800°C for 1 h coarsens the dispersoids to about 5 μm in length, as visible in the scanning electron micrograph shown in Figure 6. The matrix grains are not significantly coarsened, due to dispersoid pinning effects. However, due to this pinning, a large proportion of the dispersoids are now in grain boundaries, as can be seen in Figure 7. Figure 7 also illustrates the significant variation in the size of the boride dispersoids in these materials. The uneven size distribution of borides most likely results from localized differences in solidification rate in the EBSQ flakes.

After an anneal of 1000°C for 1 h, nearly all the borides become coarse and are located at grain boundaries. Substantial coalescence of dispersoids

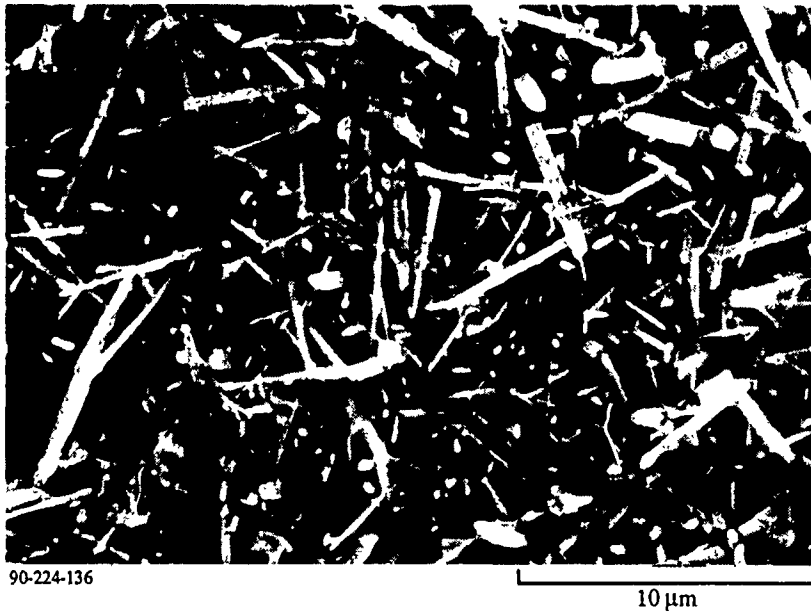**Figure 4. SEM micrograph of as-EBSQ'd microstructure of Ti-1.5B.**

Figure 5. TEM micrograph of as-EBSQ'd microstructure of Ti-1.5B.
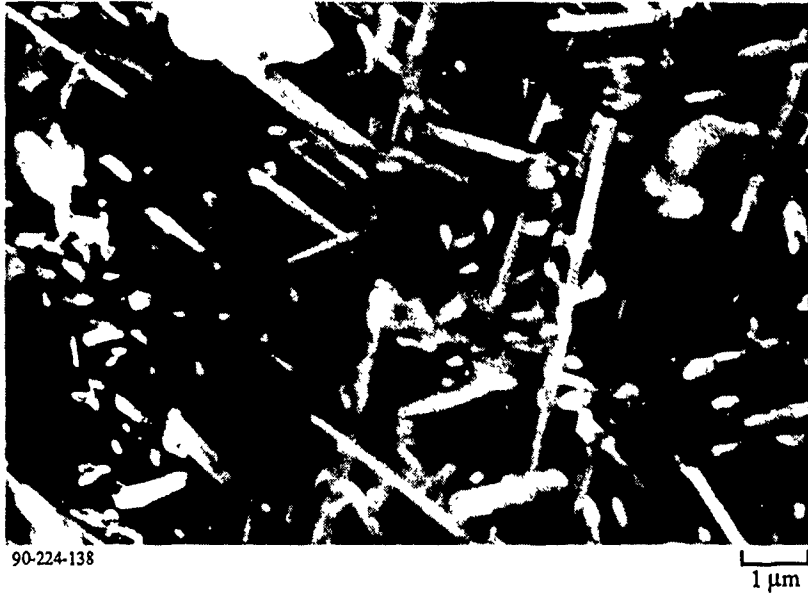
10

90-224-138

1 μm

Figure 6. Microstructure of Ti-1.5B, after 800°C/1 h anneal.

11

(a)

1 μm

(b)

90-224-139

1 μm

Figure 7. Microstructure of Ti-1.5B, after 800°C/1 h anneal; (a) small boride region,
(b) large boride region.

occurs, occasionally resulting in blocky, non-acicular borides, such as those visible in Figure 8.

At 1200°C, the alloy transforms to beta which upon cooling to room temperature transfers to martensite. Because of high diffusion rates in beta phase, the boride particles coarsen significantly and become nearly equiaxed TiB particles. There is no evidence of any residual acicular TiB. The microstructure of this material is shown in Figure 9.

3.1.1 Fine Structure of TiB Precipitates in Ti

TiB has an orthorhombic crystal structure, with the Structurbericht designation B27. The lattice parameters are $a_0 = 0.456$ nm, $b_0 = 0.612$ nm, and $c_0 = 0.306$ nm. A distinct orientation relation exists between these precipitates and the Ti matrix, namely, $(020)_{TiB} || (11\bar{2}0)_{Ti}$, $(200)_{TiB} || (1\bar{1}02)_{Ti}$ and $[001]_{TiB} || [1\bar{1}0\bar{1}]$. This relation is shown schematically in Figure 10. The long direction of the acicular precipitates was found to be the [100] direction. A high density of faults parallel to (020) in the borides was observed and is clearly visible in Figure 11a. Frequency analysis of the image in Figure 11a revealed that some of the faults have a spacing of as small as ~0.526 nm, which indicates that in some regions nearly every (020) plane is faulted because the spacing of these planes is 0.306 nm. The arrangement of atoms within a typical boride is shown in Figure 10.

3.2 Microstructure of Ti-36Al-1.5B

Titanium aluminides with 23 to 38 wt% Al form two-phase alloys containing α_2 and γ in both highly ordered lamellar colonies, as well as regions of equiaxed grains. In the rapidly solidified condition, the lamellar colonies are somewhat disordered, revealing a high level of strain contrast in TEM. Such a region is seen in Figure 12. In Ti-36Al-1.5B, the boron combines with Ti to form TiB_2 dispersoids. The dispersoids are less densely distributed throughout the matrix than in the case of pure Ti, and the dispersoids have an acicular morphology, with a hexagonal cross section.

After annealing at 800°C for 1 h, the strain contrast is substantially reduced, as seen in Figure 13. The grains show little growth, but the

90-224-140

1 μm

Figure 8. Microstructure of Ti-1.5B, after 1000°C/1 h anneal.

90-224-141

500 nm

Figure 9. Microstructure of Ti-1.5B, after 1200°C/1 h anneal.

$(020)_{TiB}\|(11\bar{2}0)_\alpha$

$(220)_{TiB}$

Boron atoms

Ti atoms

$[100]_{TiB}$

$(020)_{TiB}$
fault plane
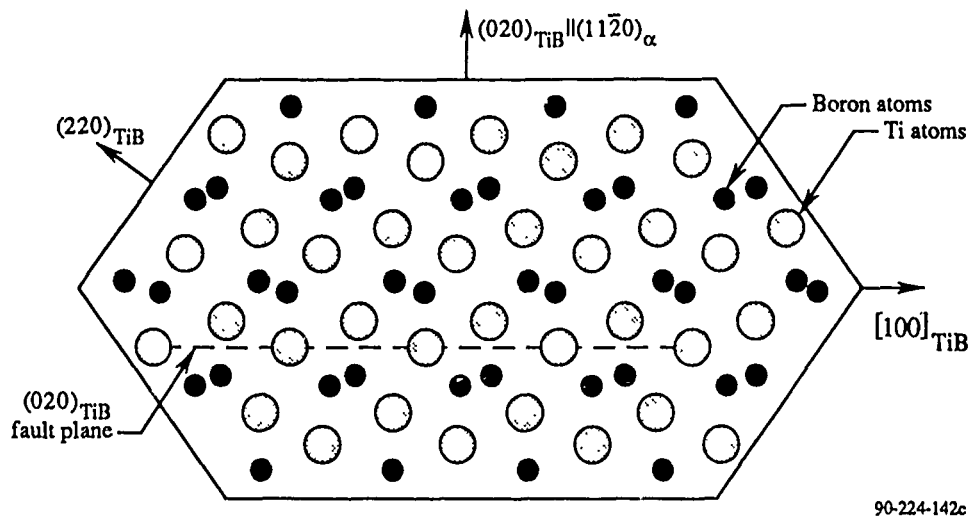
90-224-142c

Figure 10. Typical TiB morphology in α-Ti and Ti_3Al. Boride as
viewed from the $[001]_{TiB}\|[1\bar{1}0\bar{1}]_\alpha$ direction.

50 nm
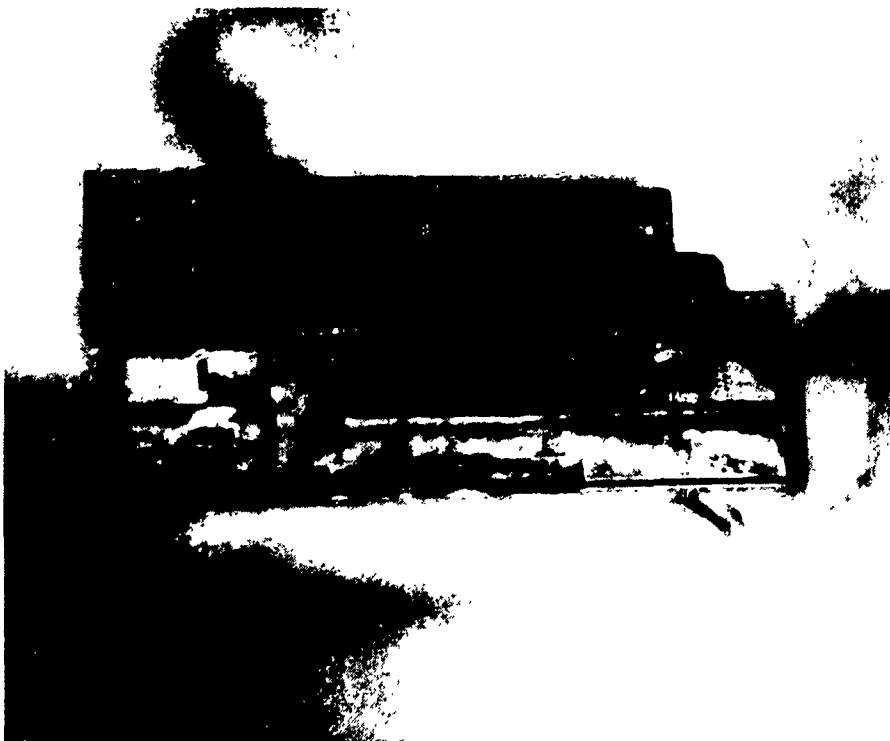
90-224-143

100 nm

Figure 11. Typical boride dispersoid morphology in (a) Ti-1.5B and (b) Ti-36Al-1.5B.

90-224-144

0.5 μm

Figure 12. TEM micrograph of as-EBSQ'd microstructure of Ti-36Al-1.5B.

90-224-145

200 nm

Figure 13. Microstructure of Ti-36Al-1.5B, after 800°C/1 h anneal.

17

density of TiB$_2$ dispersoids is higher. The annealed alloy contains a high density of small dispersoids about 0.1 μm long, indicating that a certain amount of B remains in solution after rapid solidification. The dispersoids have an acicular, or in some cases an equiaxed, hexagonally faceted structure. Figure 11a and 11b show details of boride morphologies in Ti and TiAl, respectively. The TiB$_2$ precipitates in TiAl were elongated in the [0001] direction, with faceting occurring on the (1$\bar{1}$00) prism planes. Although no orientation relation was found between the precipitates and the matrix, the strain contrast visible around the TiB$_2$ precipitate in Figure 11b indicates that some degree of coherency must exist between the precipitates and the matrix.

At 1000°C, grain growth takes place. The lamellar colonies are now distinct, with well-defined layers of α_2 and γ. The dispersoids have coarsened slightly and generally have equiaxed, faceted morphologies. Dislocations are invariably associated with the dispersoids, so it is likely that pipe diffusion plays a significant role in the growth of these dispersoids. The microstructure after this heat treatment can be seen in Figure 14.

At 1200°C, the grains have coarsened to 1 - 10 μm in diameter (Figure 15). The dispersoids show no significant growth, and the density of dispersoids is slightly higher. The dispersoids have equiaxed, faceted morphologies.

3.3 Microstructure of Ti-1.25Er

Rapidly solidified Ti-1.25 (wt%) Er has a single-phase martensitic microstructure, with Er either remaining in solution or forming small clusters of Er$_2$O$_3$ (Figure 16).

After annealing at 800°C for 1 h, virtually all of the martensite transforms to α-Ti and the Er precipitates out in the form of spherical Er$_2$O$_3$ dispersoid particles. These dispersoids are 10 - 100 nm in diameter and are uniformly distributed. The dispersoids tend to form along prior martensite plate boundaries, although not exclusively. The matrix grain size ranged from 10 to 50 μm, with equiaxed morphology. These features can be seen in Figure 17.
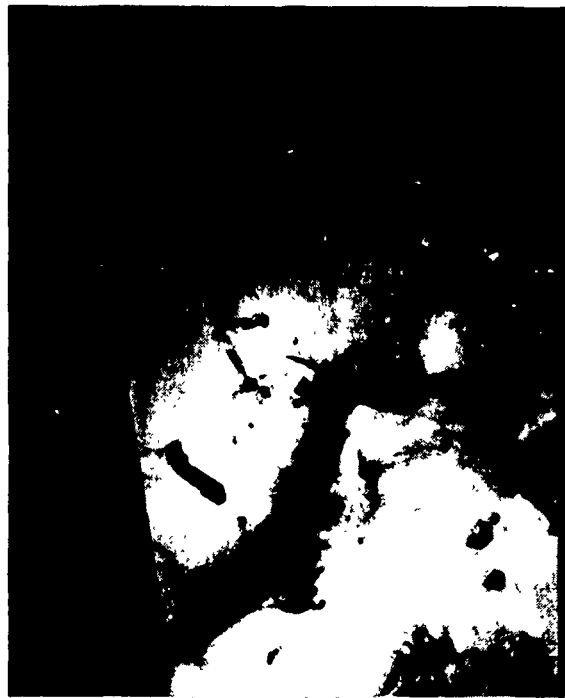
Figure 14. Microstructure of Ti-36Al-1.5B, after 1000°C/1 h anneal.

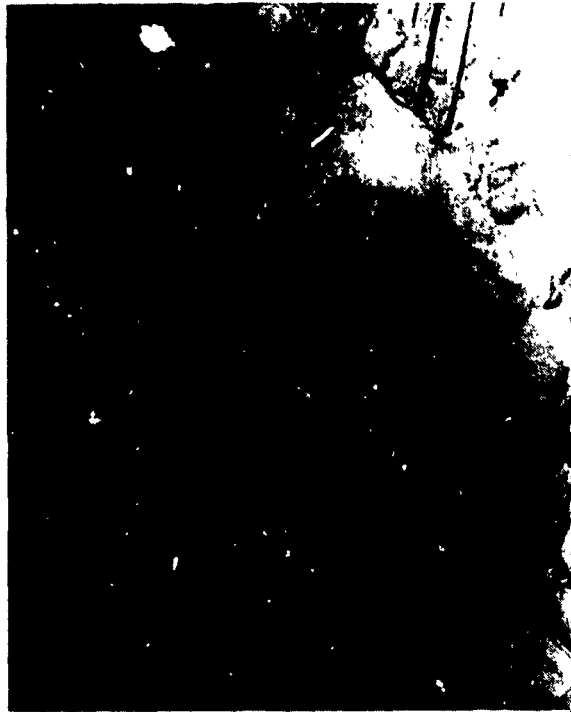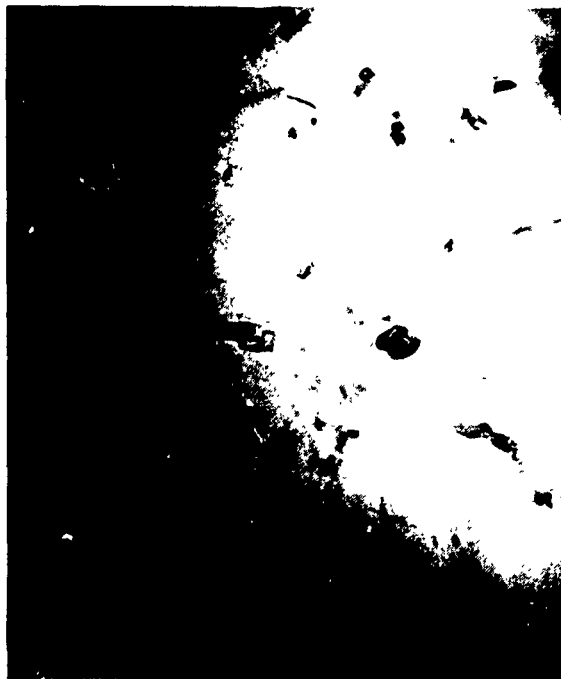**Figure 15. Microstructure of Ti-36Al-1.5B, after 1200°C/1 h anneal.**

19

90-224-148

2 μm

Figure 16. As-EBSQ'd microstructure of Ti-1.25Er.

90-224-149

2 μm

Figure 17. Microstructure of Ti-1.25Er, after 800°C/1 h anneal.

20

At 1000°C, the α-Ti grains are frequently elongated, with lengths on the order of 100 μm (Figure 18). The grain boundaries are planar, with a low concentration of dispersoids in them, indicating that they are low-energy, probably twin, boundaries. The dispersoids are no longer evenly distributed, but lie along previous grain boundaries and generally show cuboidal morphology. The dispersoids now average 50 nm in diameter with some large, faceted dispersoids attaining 500 nm diameters.

3.4 Microstructure of Ti-36Al-2Er

Figure 19 shows the as-rapidly solidified microstructure of this alloy which contains a mixture of α_2 and γ phases and is similar in microstructure to the Ti-36Al-1.5B alloy. The Er_2O_3 dispersoids display more diverse morphology in this alloy than in the Ti-1.25Er alloy. The Er_2O_3 dispersoids vary considerably in size, with spherical particles ranging from 20 - 500 nm in diameter. Some of the dispersoids form roughly square platelets with no clear orientational relation to the matrix. The large dispersoids are generally surrounded by a dispersoid-free zone. In addition, the lamellar, two-phase regions in the matrix contain far fewer dispersoids than the equiaxed regions.

At 800°C, the microstructure remains much the same as in the rapidly solidified state. The dispersoids coarsen, and the general strain contrast is reduced, but no major changes take place (see Figure 20).

At 1000°C, some large dispersoids, on the order of 5 μm, appear, frequently at grain boundaries. In addition, a high density of small (10 - 50 nm), oriented Er_2O_3 dispersoids form, frequently observed lying on {111} γ stacking faults. Figure 21 shows a large stacking fault containing a number of these dispersoids; they are always associated with dislocations and form faceted platelets, with all facets of the platelets parallel to {110} planes in the γ matrix. When viewed in a direction parallel to {110} planes in the γ matrix, the platelets exhibit distinct parallel Moiré fringes, as can be seen in Figure 22. Parallel Moiré fringes are produced by the superposition of parallel planes with different planar spacings, and they lie parallel to the planes producing them. Using the measured spacing of the Moiré fringes, $d_M = 1.14$ nm, and the known spacing of {110} planes in

Figure 18. Microstructure of Ti-1.25Er, after 1000°C/1 h anneal.

Figure 19. As-EBSQ'd microstructure of Ti-36Al-2Er.
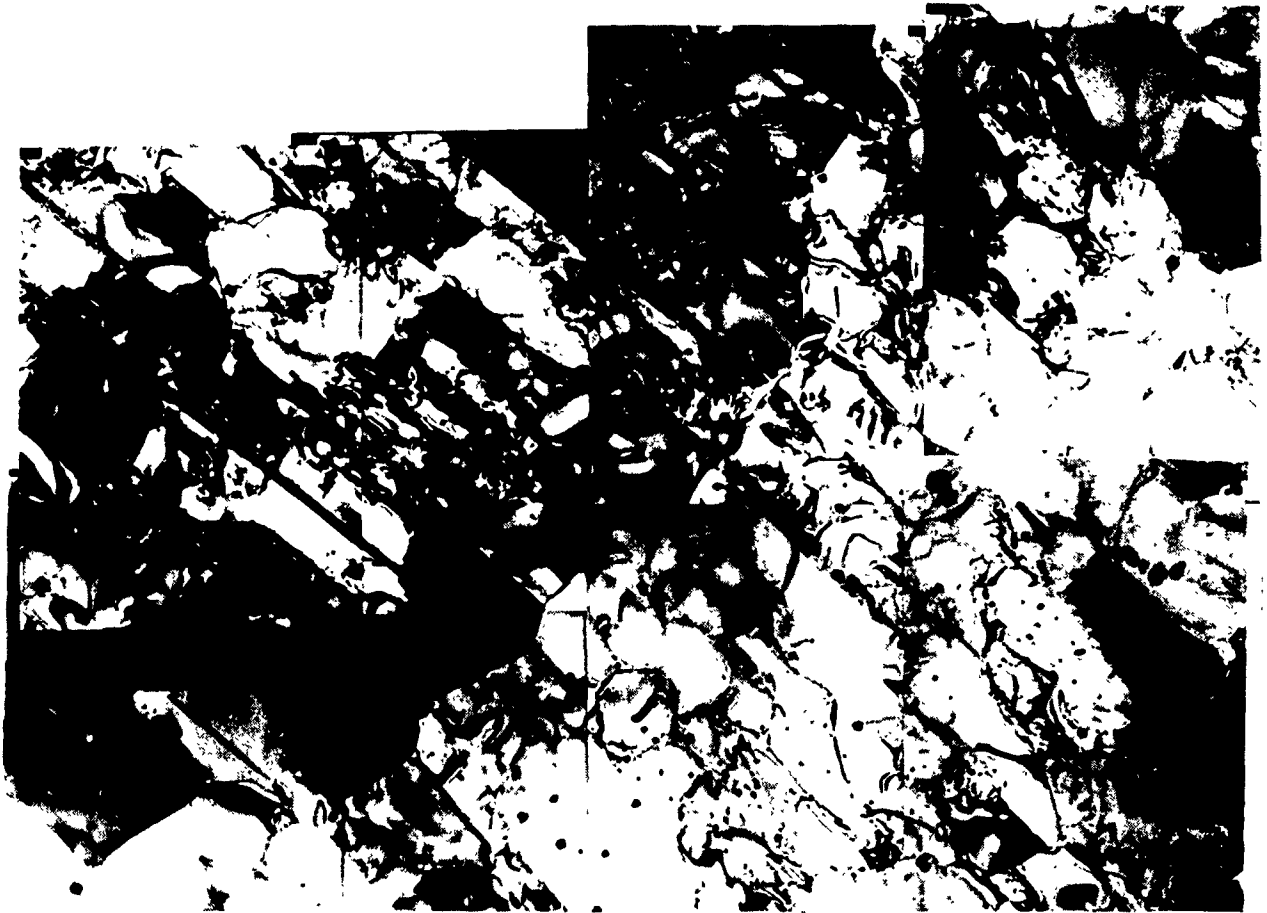
90-224-152

1 μm

Figure 20. Microstructure of Ti-36Al-2Er, after 800°C/1 h anneal.

90-224-153
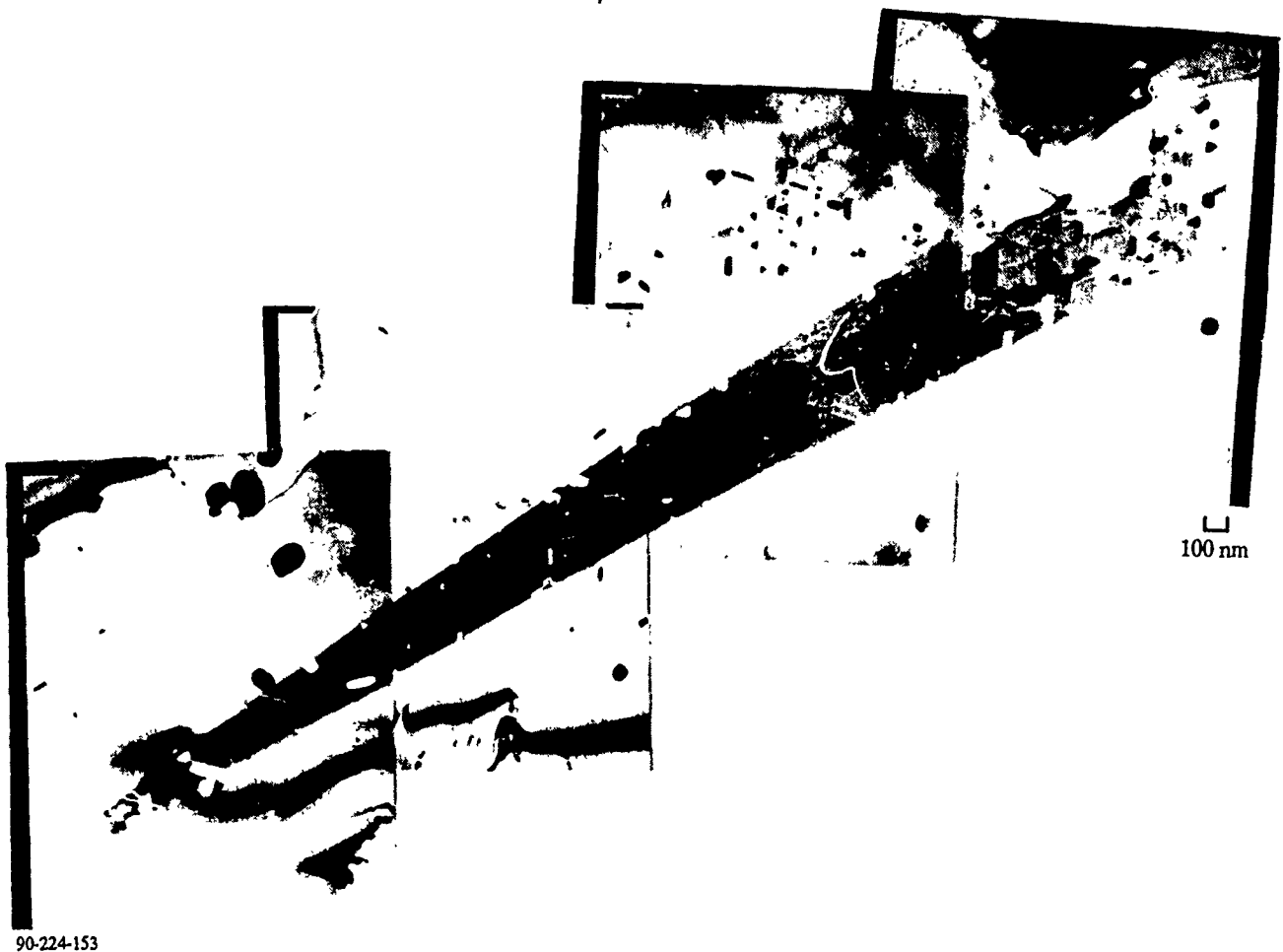
Figure 21. Microstructure of Ti-36Al-2Er, after 1000°C/1 h anneal.

90-224-154

200 nm

Figure 22. Faceted Er$_2$O$_3$ precipitates in 1000°C/1 h annealed Ti-36Al-2Er
showing Moiré fringes.

γ, d_γ = 0.281 nm, the spacing of the planes in the Er_2O_3 platelet, d_E, can be determined:

$$d_E = \frac{d_\gamma \cdot d_M}{d_M - d_\gamma} = 0.373 \text{ nm} .$$

The calculated spacing of the planes in the Er_2O_3 is the same, within experimental error, as spacing of {220} planes in Er_2O_3 (0.371 nm). There-fore, {110} planes in γ are parallel to {110} planes in the Er_2O_3 precipi-tates. The fact that precipitates lying in {111}γ planes show threefold symmetry (see Figure 21) implies that the precipitate/matrix orientation relation is cubic, i.e., (100)γ||(100)Er_2O_3, [(010)γ||(010)Er_2O_3], and (001)γ||(001)Er_2O_3.

3.5 Microstructures of Niobium Alloys

Typical as-cast microstructures are illustrated in Figures 23-26. The rare-earth-containing alloys show large, spherical particles of rare earths and significant segregation of the rare earths. The carbon-containing alloys show coarse carbide platelets, which neutron diffraction studies have shown to be the Nb_2C phase.

Figures 27a and 27b show the cross sections of flakes produced by electron-beam melting and splat quenching. For the binary Nb-2La alloy (Figure 27a) the microstructure consists of columnar grains which have grown completely through the thickness of the ribbon. This microstructure is typical of ribbons in which partitionless solidification has occurred during the entire solidification process. For the ternary Nb-15Hf-1Y ribbon, how-ever, a transition from the columnar partitionless-solidification structure to a partitional cellular/dendritic structure is observed approximately halfway through the ribbon thickness (Figure 27b). This type of transition, typically observed in alloy ribbons, reflects the variation in cooling rate with the thickness of a ribbon. Midway through the ribbon thickness, the solidification-front velocity is not sufficiently fast for complete solute trapping, and segregation occurs. For the case of the Nb-15Hf-1Y ribbon, this segregation is probably due to coring, with the interdendritic regions becoming enriched in the solute element Hf.

(a)   (b)

90-224-221   10 μm   10 μm
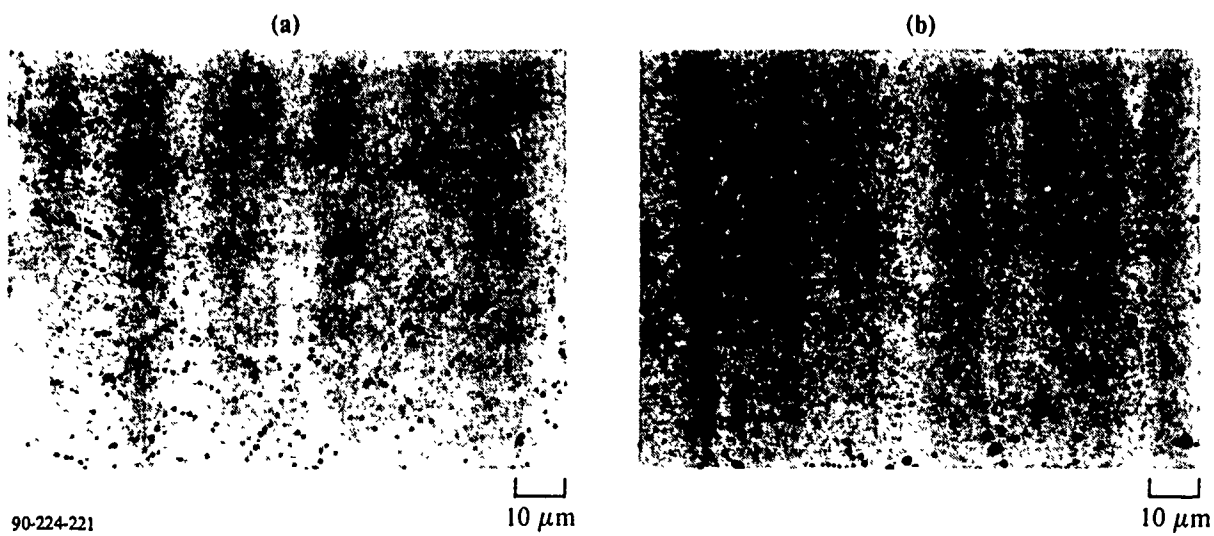
Figure 23. As-cast microstructures of (a) Nb-2La and (b) Nb-15Hf-2La alloys.

(a)   (b)

90-224-222   10 μm   10 μm
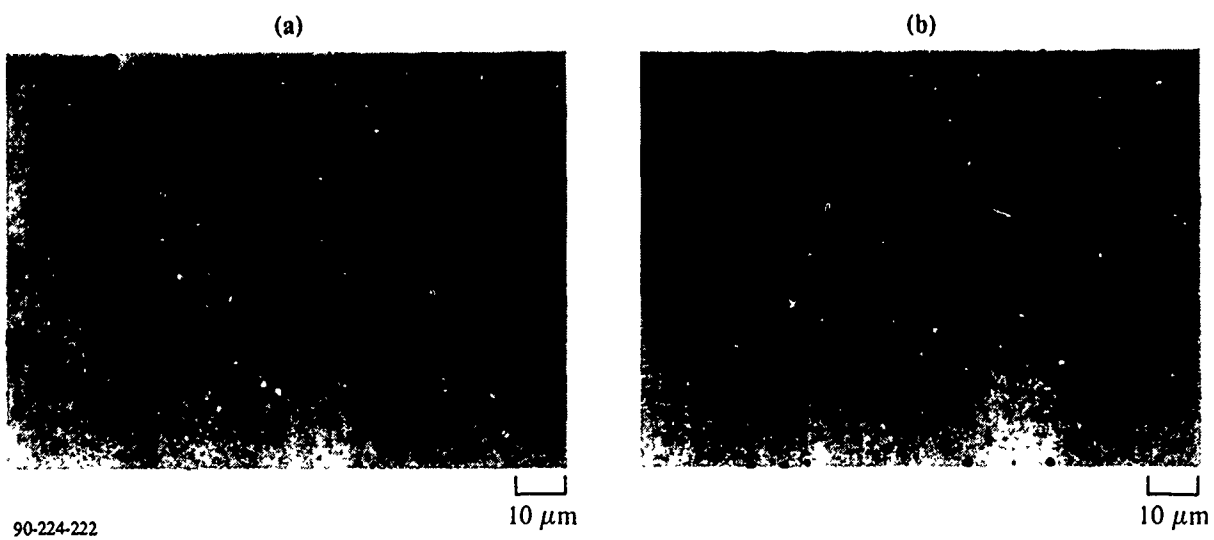
Figure 24. As-cast microstructures of (a) Nb-15W-2La and (b) Nb-30W-2La alloys.

27

(a)

(b)

10 μm

10 μm

90-224-223
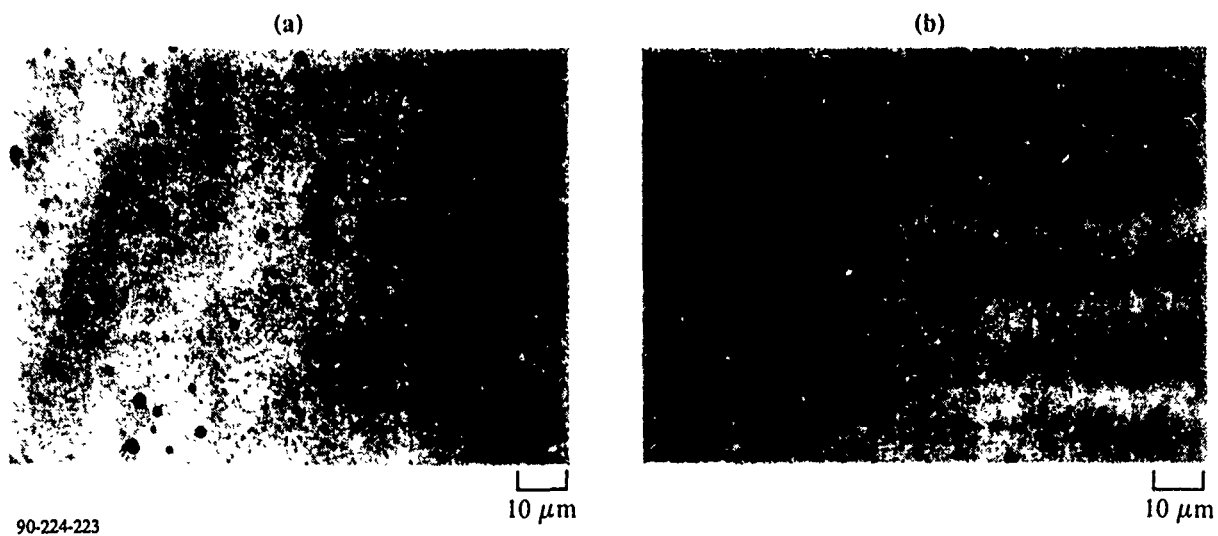
Figure 25. As-cast microstructures of (a) Nb-1Y and (b) Nb-15W-1Y alloys.

50 μm

90-224-219

Figure 26. As-cast microstructure of Nb-0.2C alloy.

28

(a)
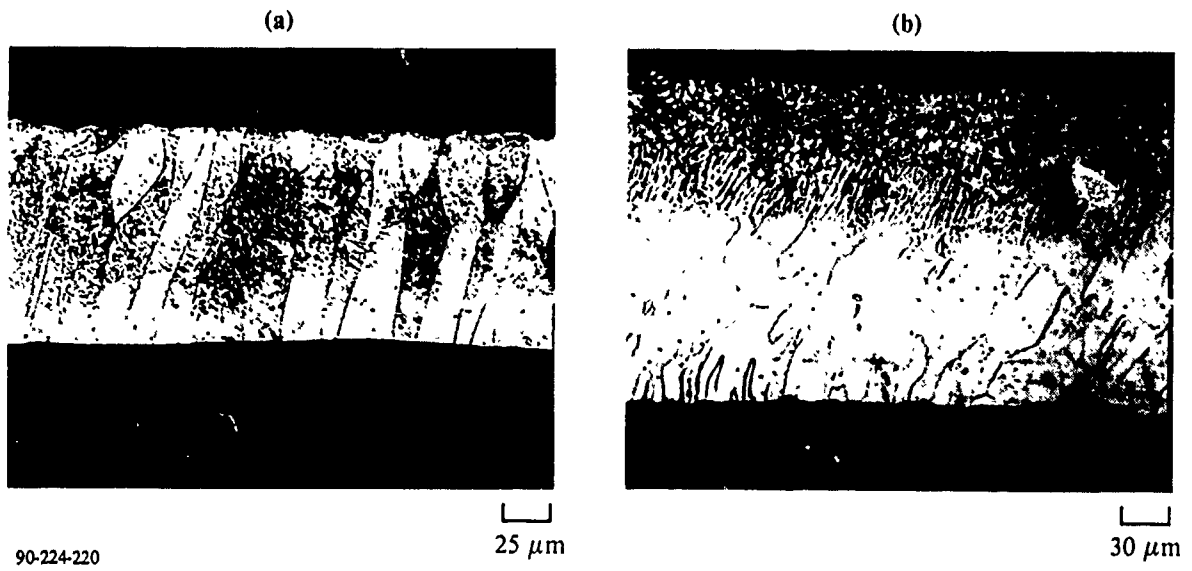
(b)

90-224-220

25 μm

30 μm

Figure 27. Microstructures of electron beam melted/splat quenched flakes of (a) Nb-2La and (b) Nb-15Hf-1Y alloys.

4. STRUCTURE OF SPECIAL GRAIN BOUNDARIES IN THE Ti-36Al MATRIX

The microstructure of alloys near Ti-36 (wt%) Al consists of colonies of parallel γ and α_2 lamellae separated by equiaxed grains of γ (e.g., Figures 12 and 20). Orientation relationships across various grain boundaries were determined using diffraction patterns (DPs) formed by positioning the selected-area diffraction (SAD) aperture to include electrons scattered by the adjacent grains and their interface. Several special relationships were observed and will be discussed below.

A high magnification transmission electron micrograph of a typical lamellar colony is shown in Figure 28. Adjacent lamellae in the lamellar colonies exhibit several well-defined orientational relations. The lamellar interface plane was found in every case to be (111) in γ and (0001) in α_2, as has previously been observed (Reference 5). The first orientational relation can be derived from the DP in Figure 29. The orientational relation is that of the simple twin in γ, commonly reported in materials with the $L1_0$ structure (References 6,7). The twin is related to the matrix in this case by the rotation

$$R_1 = 1/3 \begin{bmatrix} \bar{1} & 2 & 2 \\ 2 & \bar{1} & 2 \\ 2 & 2 & \bar{1} \end{bmatrix} .$$

The orientational relation between γ and α_2 lamellae can be deduced from the DP shown in Figure 30. It is found to be $(0001)\alpha_2||(111)\gamma$, $\langle 11\bar{2}0 \rangle\alpha_2||\langle 110 \rangle\gamma$, as reported earlier by Blackburn et al. (Reference 5). The $(0001)\alpha_2$ and $(111)\gamma$ planes match with a small misfit, so the majority of the grain boundary energy must arise from the changes in the atomic coordination that occur across the boundary. The DP in Figure 30 includes scattering from three adjacent grains, forming a $\gamma/\alpha_2/\gamma$ sandwich structure similar to that depicted in Figure 31. The DP reveals that the γ grains on either side of the central α_2 lath are related by the twinning rotation R_1. The γ/α_2 orientational relation can also be deduced from Figure 32, which is a small segment of Figure 31 magnified and filtered to enhance atomic periodicities captured in the image. The $(001)\gamma$ planes can be seen to the left

90-224-155

100 nm

Figure 28. Details of a two phase α_2/γ lamellar colony in Ti-36Al-1.5B.

31

(b)
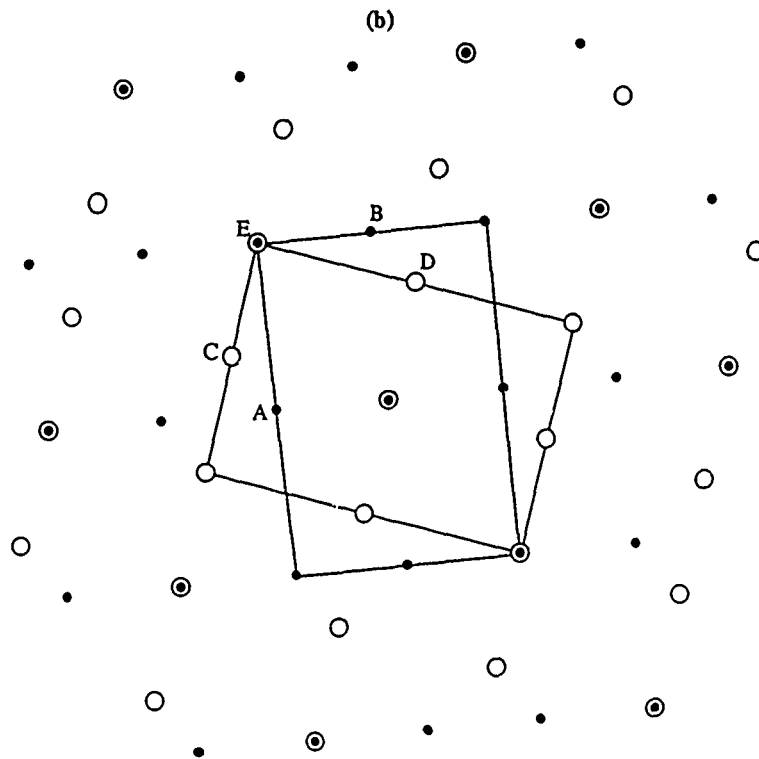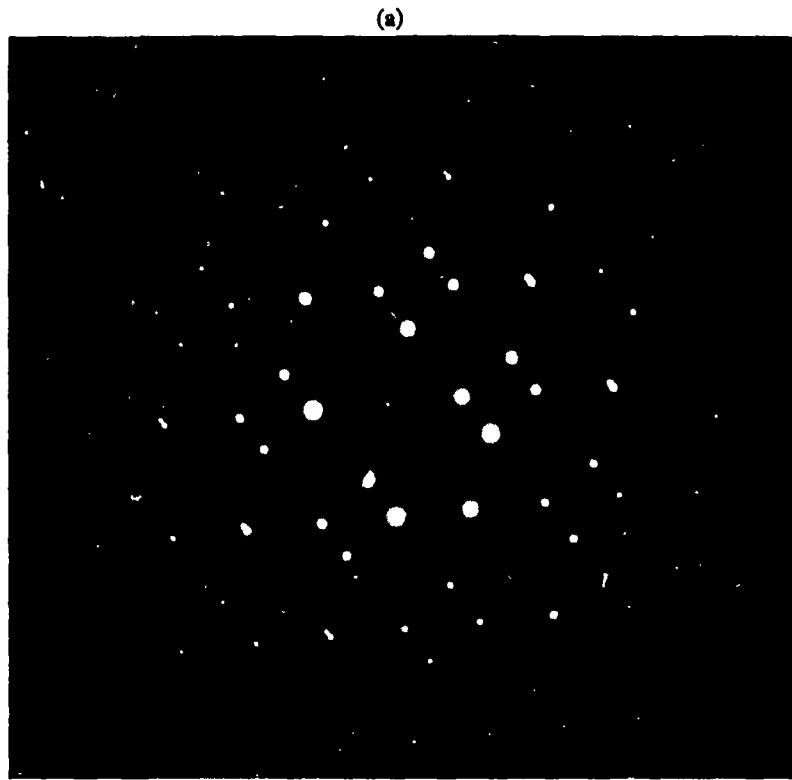
90-224-156

Figure 29. Diffraction pattern from the ordered γ twin: (a) actual DP,
(b) schematic of DP.
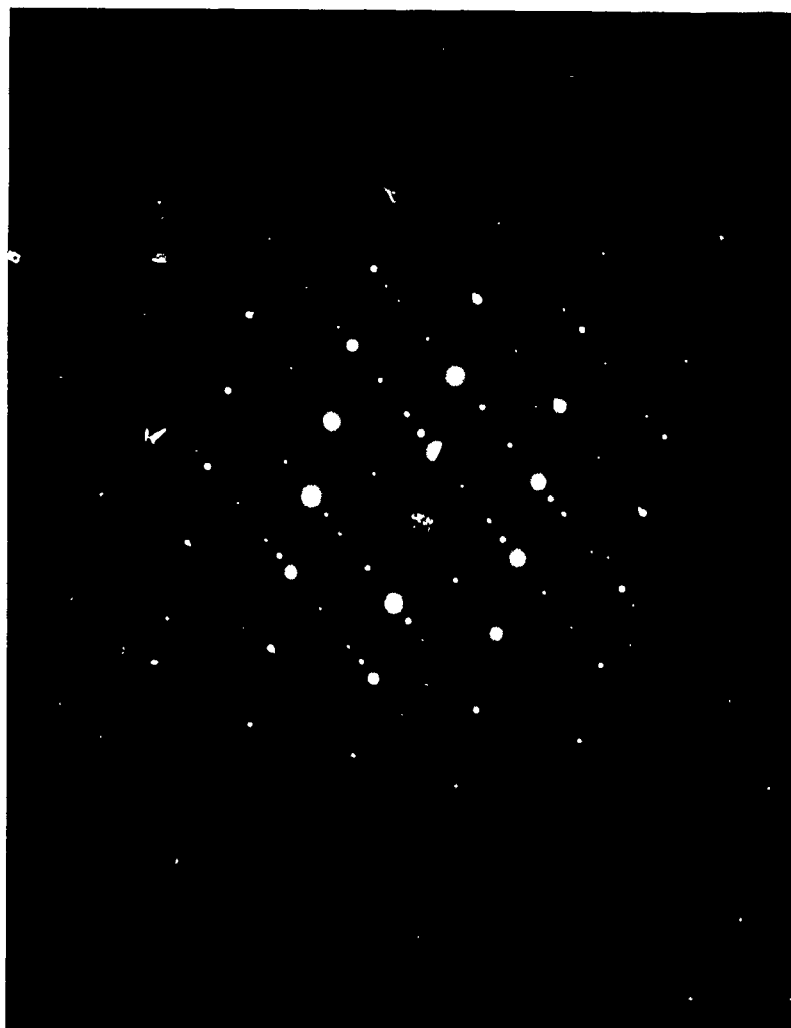
90-224-157

Figure 30. Diffraction pattern from adjacent α_2 and γ lamellae.

90-224-158

10 nm

Figure 31. High-resolution TEM micrograph of the $\gamma/\alpha_2/\gamma$ sandwich structure.

90-224-159a

3 nm
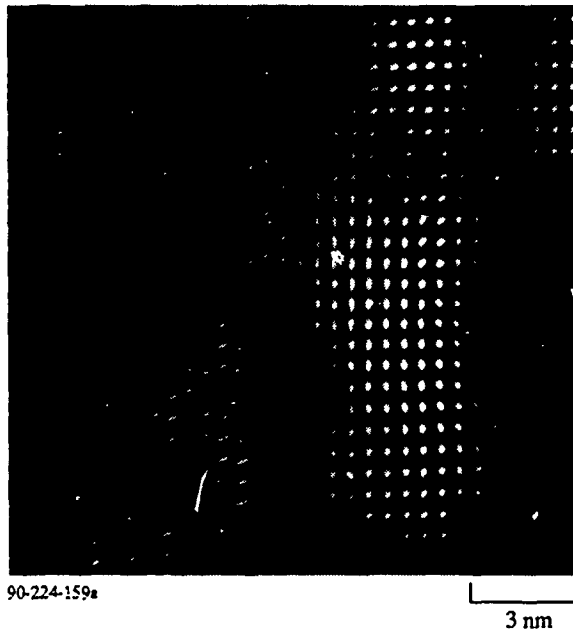
Figure 32. Segment of the γ/α_2 interface, magnified and Fourier filtered. Viewing direction is $< 110 \,]\, \gamma \,\|\, < 11\bar{2}0 > \alpha_2$.

Note: γ grain is on the left hand side, α_2 grain on right.

of the interface, and the $(1\bar{1}00)$ and $(0001)\alpha_2$ planes on the right. The γ/α_2 orientation relation can be determined by analyzing the angles between these planes and the interface. Note that the spacing of the $(110)\gamma$ planes is 0.141 nm, which is below the resolution of the TEM used for this specimen; thus, only one set of planes is resolved in the γ grain.

A third structure observed in the lamellar colonies is a sandwich structure that is similar to a pseudo-twin. A typical example is shown in Figure 31. The structure consists of three lamellae, two γ lamellae separated by a thin lath of α_2. Both γ/α_2 interfaces show the usual orientational relation, except that one has $\langle11\bar{2}0\rangle||\langle110\rangle$, and the other $\langle11\bar{2}0\rangle||\langle101\rangle$. This relation implies that the α_2 layer, which is usually observed to be quite thin (10-50 nm), separates two γ lamellae related by a rotation

$$R_2 = 1/3 \begin{bmatrix} 2 & 2 & \bar{1} \\ \bar{1} & 2 & 2 \\ 2 & \bar{1} & 2 \end{bmatrix} .$$

This relationship can be thought of as a twinning wherein the twin plane reflects the atomic positions of the matrix into the twin in the usual way, but the species of atoms that occupy the atomic positions are not correctly reflected from the matrix into the twin. Therefore, the γ grains are in a pseudo-twin orientation (Reference 8). As can be seen in Figure 31, the γ laths are separated by a lamella of α_2 that is wide enough to preclude any direct interaction between them; thus this structure is not an actual pseudo-twin, although it is geometrically similar.

Positioning a SAD aperture over the entire three-lamella structure forms the DP in Figure 33a, taken with the electron beam parallel to the $[11\bar{2}0]\alpha_2$ direction. Due to the $L1_0$ ordered structure of γ, the $\langle110]$ DP and the $\langle101]$ DP are not identical. The $\langle110]$ pattern is twice as dense at the $\langle101]$ DP, and therefore the pseudo-twin relationship between the γ grains can be deduced from the DP shown in Figure 33. Figure 33b schematically shows the origin of the diffracted spots in Figure 33a. The presence of a thin layer of α_2 results in the faint $\langle11\bar{2}0\rangle\alpha_2$ DP superimposed on the γ
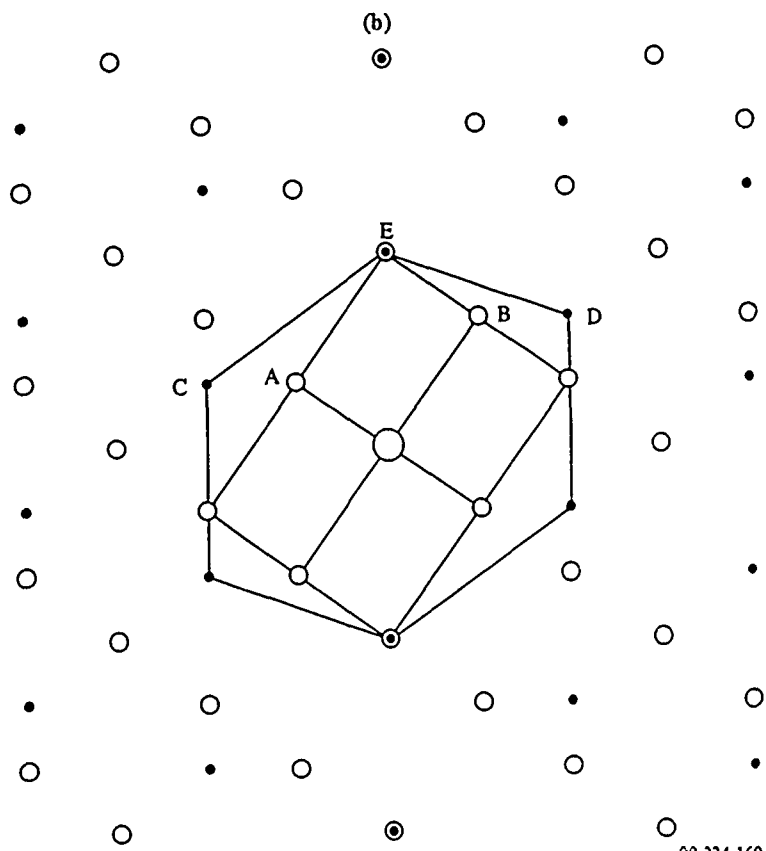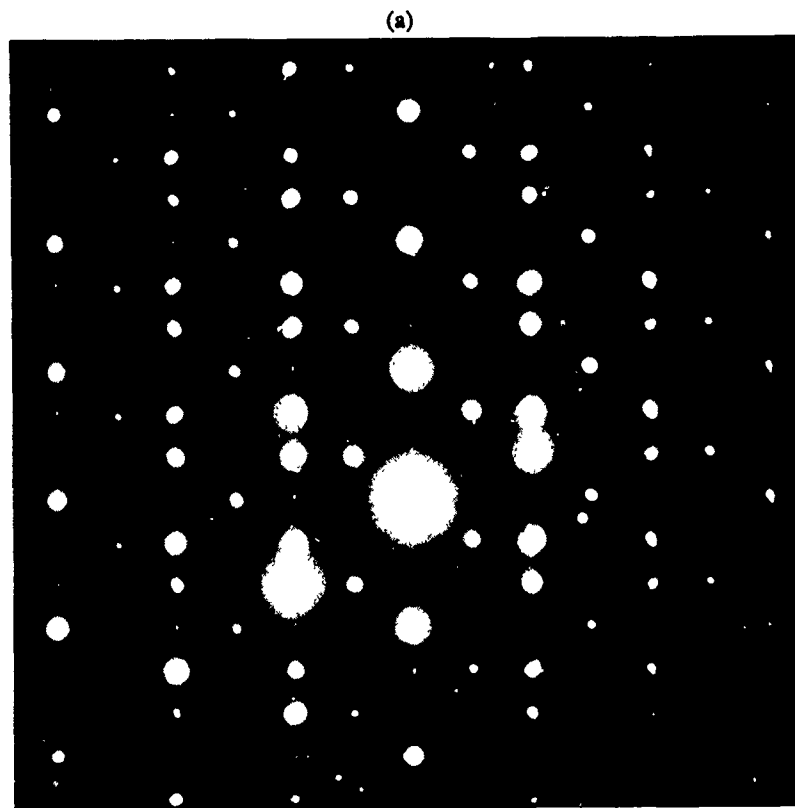
Figure 33. Diffraction pattern from the non-ordered γ twin: (a) actual DP, (b) schematic of the DP.

90-224-160

pseudo-twin DP visible in Figure 33a. In addition, there is a small tetragonal distortion between the two DPs that manifests itself in the noncoincidence of high-order reflections in Figure 33a. The three-lamella pseudo-twin-like structure thus can be recognized with certainty by the DP in Figure 33. The observations of this pseudo-twin structure corroborate the recent findings of Reference 9.

A fourth structure has been observed that is also a sandwich structure. The γ lamellae, separated by a lath of α_2, are not related by a twinning rotation in this structure. Formally, the γ lamellae are related by the rotation

$$R_3 = \begin{bmatrix} 0 & 0 & 1 \\ 1 & 0 & 0 \\ 0 & 1 & 0 \end{bmatrix} .$$

In a cubic, nonordered system, this rotation would be a symmetry operation. However, because γ has the $L1_0$ structure, this rotation is non-symmetric and introduces a change in order between the γ grains. Therefore, R_3 will be referred to as an order-changing rotation. All planes of the same type remain nearly parallel after this rotation because the tetragonality of γ is slight ($c/a = 1.025$). This parallelity is revealed by the fact that the DP's from the adjacent γ laths superimpose, as can be seen in Figure 34a, indicating that all planes in the two laths are parallel. Note that the tetragonality results in splitting of the high-order reflections, indicating that the reflecting planes deviate slightly from being exactly parallel. Figure 34b demonstrates that one of the superimposed DPs is the {101} pattern, whereas the other is the denser {110}, indicating that the order within the planes is not the same in the two γ grains. The DP analysis is shown schematically in Figure 34b. Note that the spots due to the α_2 lath are very faint because of the small amount of α_2 contributing to the DP.

Finally, nonplanar interfaces were observed within equiaxed γ regions with the adjacent γ grains related by the same order-changing rotation as above, R_3. A typical example is shown in Figure 35, and it can be seen that such interfaces contain a high density of dislocations and no preference for a specific habit plane. The rotation relating the adjacent grains was

(a)

(b)
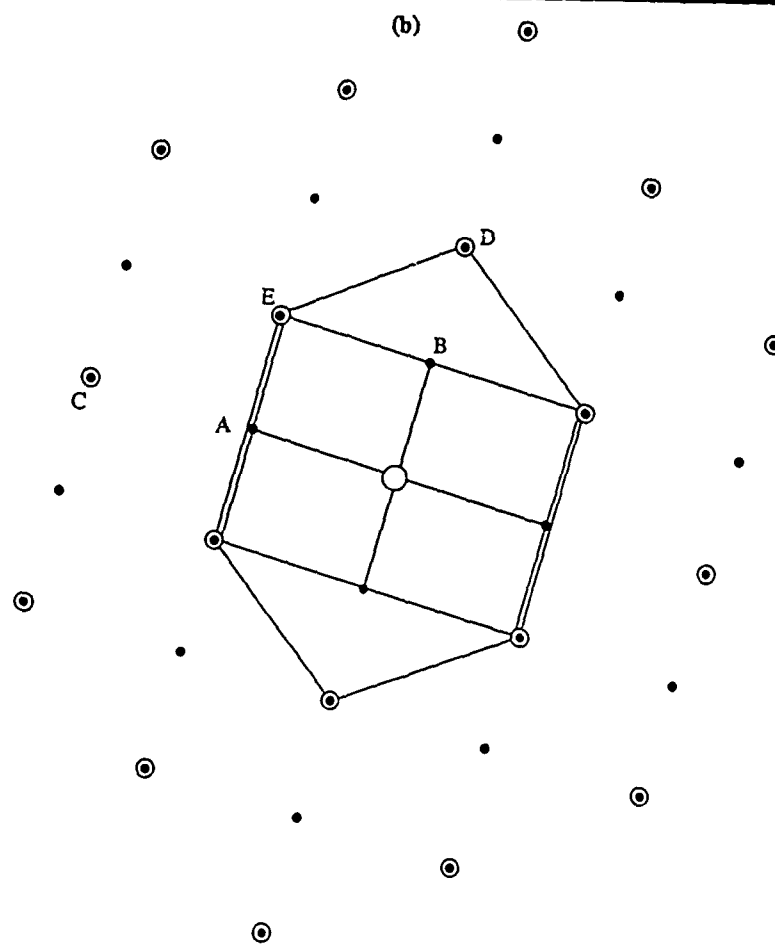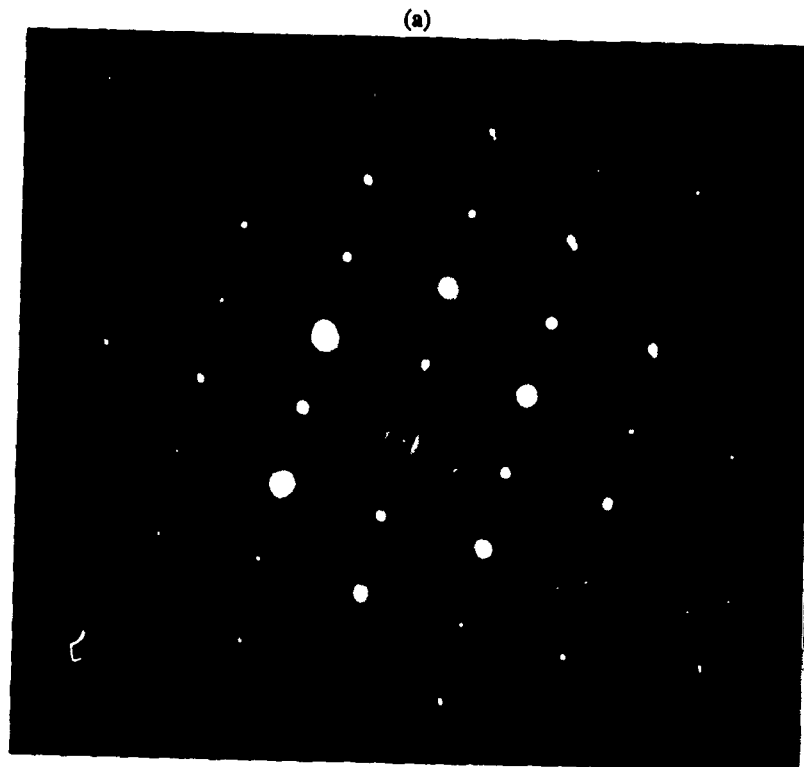
Figure 34. Diffraction pattern from the γ stacking-fault-like structure:
(a) actual DP, (b) schematic of the DP.

90-224-161

39

90-224-162a

100 nm

Figure 35. TEM micrograph of a nonplanar special grain boundary
across which ordering is changed.

determined from the $[010]\gamma$ DP in Figure 36a, shown schematically in Figure 36b.

In summary, six distinct special grain boundaries have been identified in the two-phase α_2/γ lamellar structure, where every interface is constrained to lie parallel to $(111)\gamma$, as well as one nonplanar special boundary which is found in equiaxed γ regions. These grain boundaries are the following:

(1) γ/γ twins, related by the rotation R_1 given above, i.e., the mirror twin that does not change the order within planes parallel across the interface.

(2) α_2/γ interfaces, with the orientation relation determined by Reference 5.

(3) $\gamma/\alpha_2/\gamma$ sandwich structures, where each α_2/γ interface has the above orientation relation, and the γ grains are related by the twinning rotation, R_1.

(4) $\gamma/\alpha_2/\gamma$ sandwich structures, where e ι α_2/γ interface has the above orientation relation, but the γ grai re related by the rotation R_2, i.e., they are non-mirror twins with the order within parallel planes changing across the interface. This corroborates the findings of Reference 9.

(5) $\gamma/\alpha_2/\gamma$ sandwich structures, where each α_2/γ interface has the above orientation relation, but the γ grains are related by the rotation R_3, the order-changing rotation.

(6) γ/γ interfaces in equiaxed γ regions, with the adjacent grains related by the order-changing rotation, R_3.
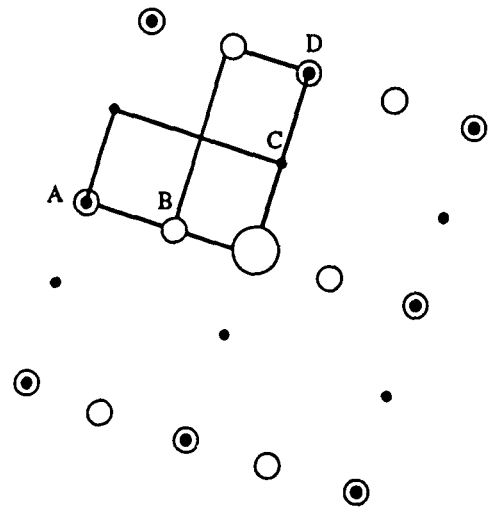
Orientation Relationship: $(200)_1 \| (001)_2, [010]_1 \| [100]_2$

A: $(200)_2$ and $(002)_1$ C: $(001)_2$
B: $(001)_1$ D: $(002)_2$ and $(020)_1$

90-224-163a

Figure 36. Diffraction pattern from a nonplanar special grain boundary in γ.

5. MECHANICAL PROPERTIES OF RAPIDLY SOLIDIFIED ALLOYS

5.1 Mechanical Properties of EBSQ Flakes

Flat tensile specimens (Figure 37) and a grip assembly (Figure 38) were used for tensile testing of small tensile specimens machined directly from EBSQ Ti alloy flakes. The alloys Ti-1C, Ti-2Er, Ti-0.5B, and pure Ti were tested at room temperature after a variety of anneals.

The stress-strain curves of rapidly solidified Ti, Ti-2Er, Ti-0.5B, and Ti-1C alloys in the rapidly solidified and heat-treated conditions are shown in Figures 39 and 40. The yield stresses and work-hardening rates are significantly higher in Ti alloys containing Er, B, and C than in unalloyed Ti.

In the as-EBSQ condition, most of the strengthening in the alloys is due to the presence of interstitial atoms, which are trapped in the lattice by the rapid solidification process. Both C and B are potent solid-solution hardeners (References 10,11), and the addition of C can be seen to strengthen the Ti considerably, at the expense of ductility (Figure 39d).

Annealing the EBSQ flakes causes the interstitially trapped atoms to come out of solution and form either Ti compounds (C and B) or oxides (Er). These finely dispersed precipitates strengthen the alloys dramatically, as shown for the B-containing alloy in Figure 41.

5.2 Mechanical Properties of Extrusions Produced with Rapidly Solidified Powders

Six alloys were selected for detailed mechanical property evaluation. Rapidly solidified powders were produced using the PAMCA technique, and then consolidated by extrusion. The extruded bars were heat treated to produce different reinforcement morphologies, and the bars were then tensile tested at 25 - 900°C.

Approximately 4 kg of powder was produced for each of the following six alloys: Ti-1B, Ti-2Er, Ti-16Al-1B, Ti-16Al-2Er, Ti-34Al-1B, and Ti-34Al-2Er. The actual compositions and interstitial impurity levels are listed in Table 1.

All alloy lots contain the desired Al and B concentrations. The Er concentrations were slightly lower than desired, but were similar in each of
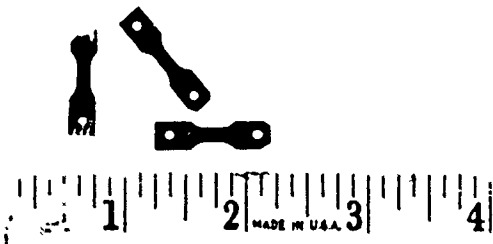
Figure 37. Tensile specimens machined from electron-beam-melted/splat-quenched flakes of Ti alloy.
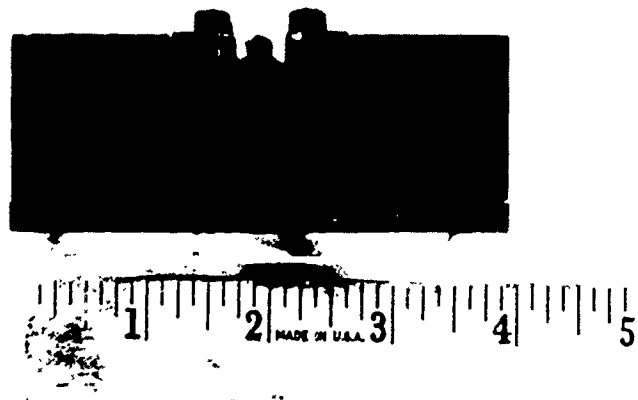
Figure 38. Grip assembly for gripping thin tensile specimens.
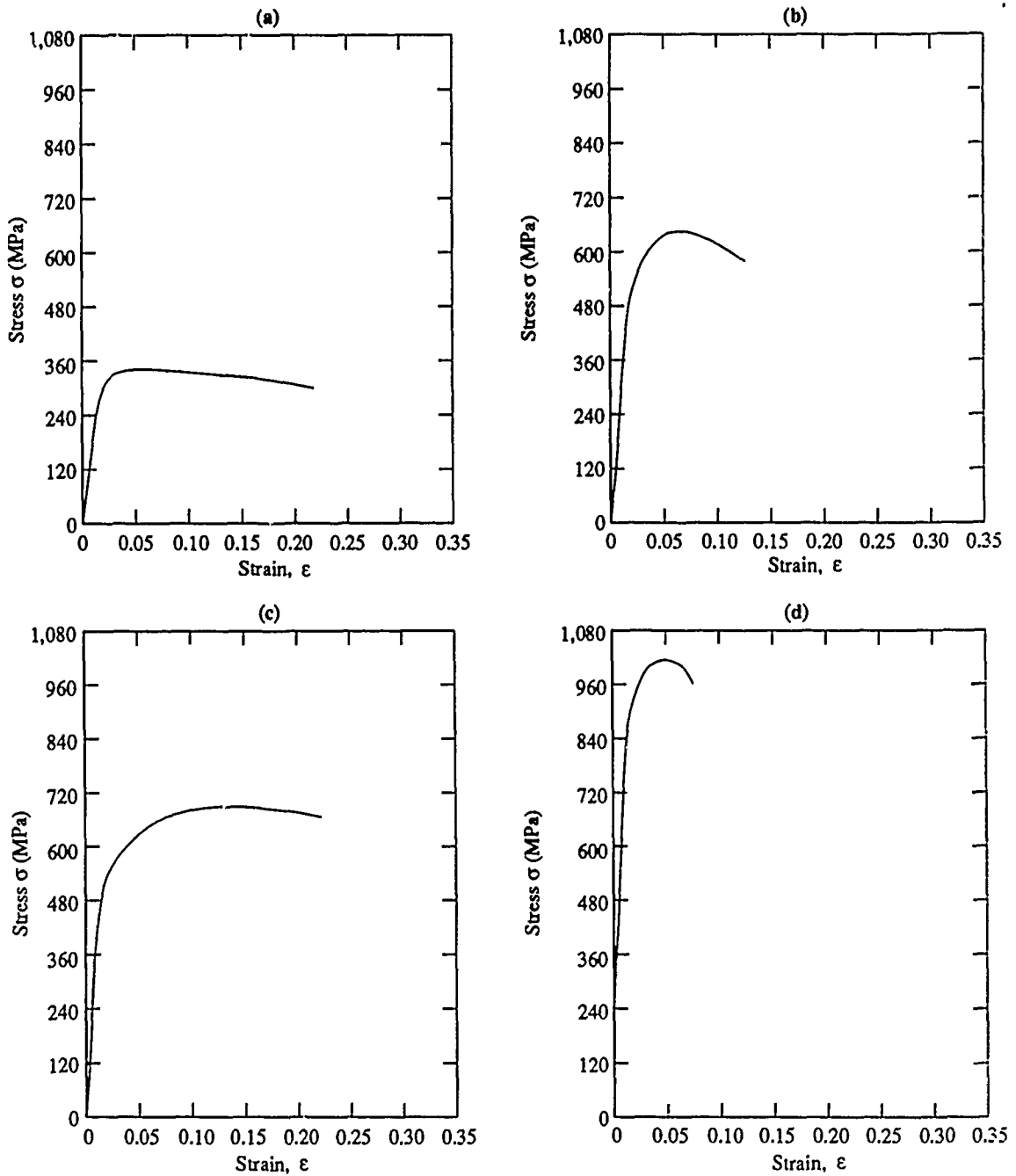
Figure 39. Stress-strain curves of rapidly solidified (a) Ti, (b) Ti-2Er, (c) Ti-0.5B, and (d) Ti-1.0C alloys.

45
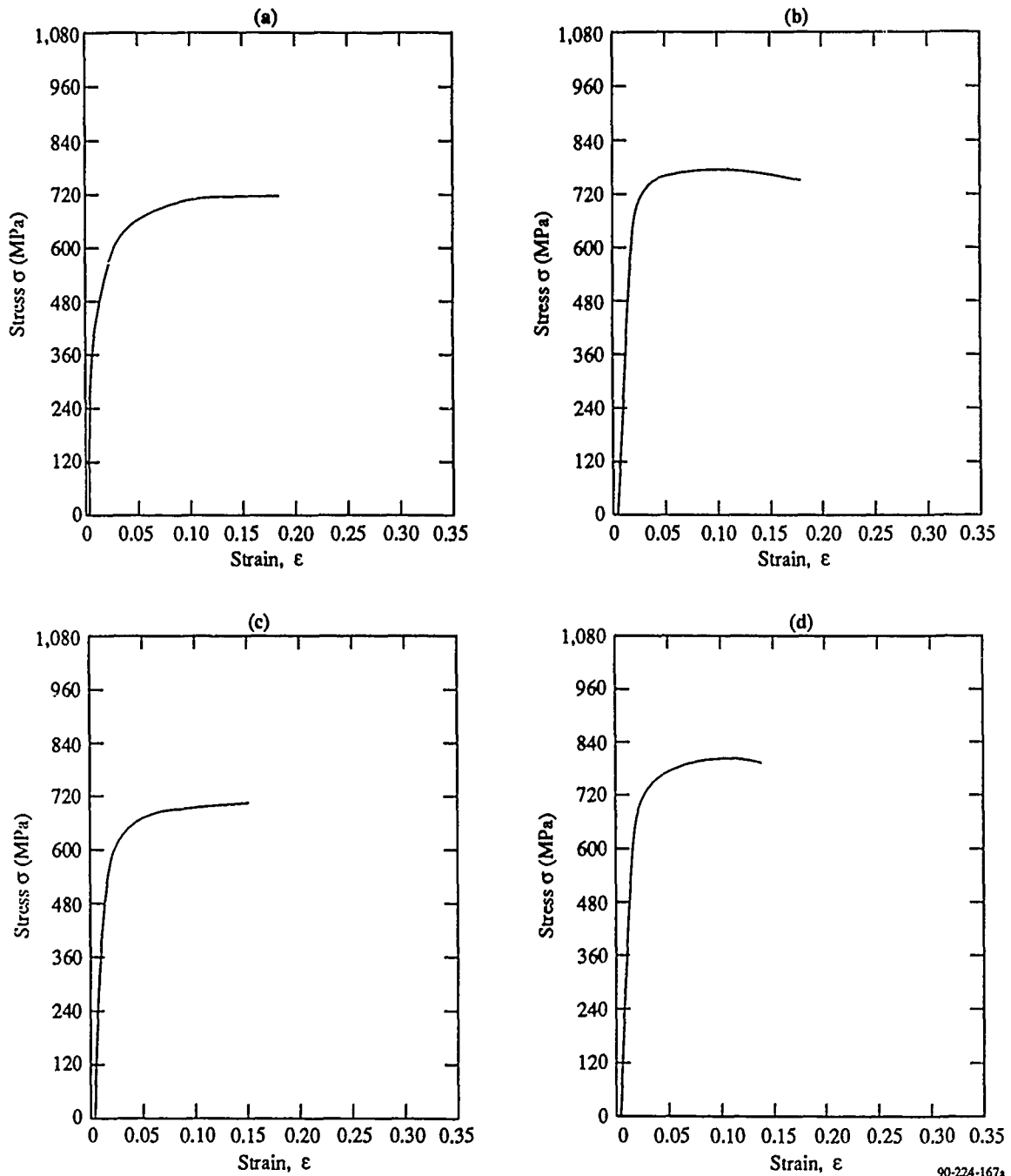
Figure 40. Stress-strain curves of rapidly solidified Ti-0.5B annealed at
(a) 700°C/2 h, (b) 810°C/4 h, (c) 800°C/18 h, and (d) 900°C/2 h.

90-224-167a
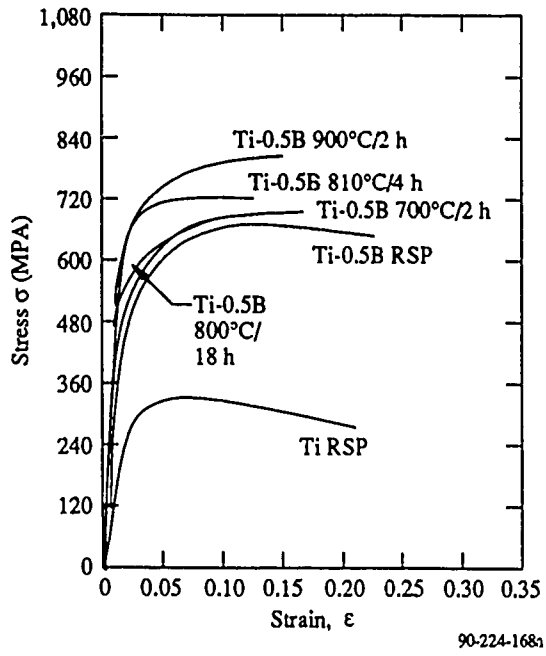
Figure 41. Comparison of stress-strain
curves of Ti and Ti-0.5B alloys.

the three Er-containing alloys. The H interstitial levels were very good; however the concentrations of O, C, and N were generally higher than expected.

The powders were packed inside thick-walled, 70-mm-diameter Ti-6Al-4V extrusion cans, vacuum outgassed, and sealed. Each can accommodated 1 kg of powder. The alloys were then extruded at the Air Force Materials Laboratory after holding at the extrusion temperature for 2 h. All alloys were extruded through a circular die with a reduction ratio of 16:1. The Ti based alloys (alloys 1 and 2) were extruded at 1000°C (1830°F), and the α_2-based alloys (alloys 3 and 4) were extruded at 1260°C (2300°F). All four of these alloys extruded very well. The γ-based alloys (alloys 5 and 6) were extruded at 1340°C (2450°F) and showed signs of breakup and a roughened surface appearance. Both extrusions, however, contained enough good material for mechanical test specimens. Button-ended tensile specimens (Figure 42) were fabricated by cylindrical grinding to a 63 finish. The specimens were then sealed in evacuated quartz capsules and heat treated. The heat treatments used in this study and the resultant microstructures are presented in Table 3.

Samples were then tensile tested in air at the following temperatures: Ti-2Er and Ti-1B at 25, 500, and 715°C; Ti-16Al-2Er and Ti-16Al-1B at 25, 600, and 815°C; Ti-34Al-2Er and Ti-34Al-1B at 25, 815, and 900°C. The results are shown in Table 4.

The boron additions to the Ti-1B alloy (alloy 1) result in a substantial increase in 25°C tensile strength and a drastic reduction in ductility at 25°C compared to unalloyed titanium, which has σ_y = 300 MPa (43 ksi) and σ_{uts} = 350 MPa (50 ksi) (Reference 12). Alloy 1 has higher strength values and much lower ductility than the EBSQ material, reported in Section 5.1; these characteristics may be due to the higher boron content of alloy 1. While strength values are considerably higher, the modulus values of alloy 1 are only marginally higher than the 103 GPa (15 Msi) value for unalloyed titanium.

Heat treatment had a minor effect on properties of alloy 1. The 1000°C/5 h/air cool (AC) heat treatment, which produced slightly coarser borides with lower aspect ratios, yielded a 15% decrease in room-temperature

0.050 R
Typical

Gradual Taper
0.062 Long

0.125

0.750

2.250

0.175

0.250

0.350

90-224-169b
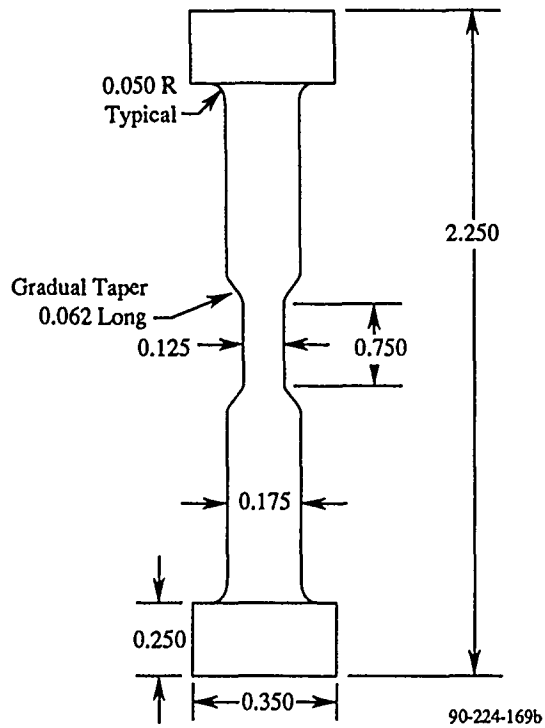
Dimensions in inches

Figure 42. Cylindrical tensile specimen geometry.

49

Table 3. Microstructural characteristics of heat-treated alloys chosen for mechanical property evaluation.

Alloy	Heat treatment	Microstructural characteristics			
Ti-2Er (~0.77 vol% Er_2O_3)	800°C/1 h/AC 1000°C/5 h 800°C/24 h	Fine (0.93 μm dia) particles in a fine Widmanstätten microstructure Coarser (1.23 μm dia) particles in a coarse Widmanstätten microstructure Coarse (1.71 μm dia) particles in a coarse Widmanstätten microstructure containing grain boundary alpha			
Ti-1B		Aspect ratio	Length (μm)	Width (μm)	Effective dia (μm)
(~3.45 vol% TiB)	800°C/1 h/AC 800°C/24 h 1000°C/5 h	4.68 5.04 3.64	5.33 5.38 5.86	1.18 1.12 1.56	3.49 3.53 3.91
Ti-16Al-2Er (~0.82 vol% Er_2O_3)	850°/1 h/AC 1100°C/5 h	Fine (1.11 μm dia) particles in an equiaxed matrix Coarser (2.17 μm dia) particles			
		Aspect ratio	Length (μm)	Width (μm)	Effective dia (μm)
Ti-16Al-1B (~3.91 vol% TiB)	850°C/1 h/AC 1100°C/5 h	3.66 2.50	9.87 8.15	2.80 3.37	6.84 5.97
Ti-34Al-2Er (~0.86 vol% Er_2O_3)	900°C/1 h/AC 1200°C/5 h + 900°C/5 h	Coarse (1.68 μm dia) particles Fine (0.95 μm dia) particles			
Ti-34Al-1B	900°C/1 h/AC	Aspect ratio	Length (μm)	Width (μm)	Effective dia (μm)
(~4.01 vol% TiB_2)	1200°C/5 h + 900°C/5 h	1.74 1.76	0.90 1.20	0.52 0.71	0.68 0.94

90-220-174c

50

Table 4. Mechanical properties of titanium alloys 1 - 6.

Alloy 1 (Ti-1B)			
Test temperature	Heat treatment		
	800°C/1 h/AC	800°C/24 h/AC	1000°C/5 h/AC
25°C YS [MPa (ksi)]	720 (104.4)	729 (105.7)	610 (88.5)
UTS [MPa (ksi)]	837 (121.4)	869 (126.0)	716 (103.8)
% Elongation	20.1	17.1	14.0
Modulus [GPa (Msi)]	105 (15.2)	122 (17.7)	112 (16.3)
500°C YS [MPa (ksi)]	476 (69.0)	674 (97.7)	384 (55.7)
UTS [MPa (ksi)]	510 (74.0)	714 (103.6)	459 (66.5)
% Elongation	4.6	9.7	8.3
715°C YS [MPa (ksi)]	155 (22.5)	220 (32.2)	174 (25.3)
UTS [MPa (ksi)]	173 (25.1)	239 (34.6)	185 (26.9)
% Elongation	17.3	20.3	11.4
Alloy 2 (Ti-2Er)			
25°C YS [MPa (ksi)]	1290 (187.1)	1326 (192.3)	1116 (161.9)
UTS [MPa (ksi)]	1352 (196.1)	1326 (192.3)	1132 (164.5)
% Elongation	1.7	0.1	0.3
Modulus [GPa (Msi)]	106 (15.4)	103 (14.9)	118 (17.1)
500°C YS [MPa (ksi)]	505 (73.3)	442 (64.1)	452 (65.5)
UTS [MPa (ksi)]	636 (92.2)	584 (84.7)	593 (86.0)
% Elongation	7.0	7.7	2.7
715°C YS [MPa (ksi)]	112 (16.3)	90 (13.1)	117 (17.0)
UTS [MPa (ksi)]	114 (16.6)	95 (13.8)	121 (17.6)
% Elongation	47	60	65
Alloy 3 (Ti-16Al-1B)			
	850/1 h/AC	1100/5 h/AC	
25°C YS [MPa (ksi)]	–	–	
UTS [MPa (ksi)]	422 (61.2)	253 (36.7)	
% Elongation	–	–	
Modulus [GPa (Msi)]	142 (20.6)	163 (23.7)	
600°C YS [MPa (ksi)]	–	–	
UTS [MPa (ksi)]	592 (85.9)	418 (60.6)	
% Elongation	0.1	–	
815°C YS [MPa (ksi)]	423 (61.4)	–	
UTS [MPa (ksi)]	440 (63.8)	429 (62.2)	
% Elongation	16.3	–	
Alloy 4 (Ti-16Al-2Er)			
25°C YS [MPa (ksi)]	–	–	
UTS [MPa (ksi)]	350 (50.7)	499 (72.4)	
% Elongation	–	–	
Modulus [GPa (msi)]	114 (16.6 Msi)	181 (26.3)	
600°C YS [MPa (ksi)]	–	–	
UTS [MPa (ksi)]	653 (94.7)	463 (67.2)	
% Elongation	0.1	–	
815°C YS [MPa (ksi)]	–	453 (65.7)	
UTS [MPa (ksi)]	148 (21.4)	521 (75.5)	
% Elongation	–	3.0	
Alloy 5 (Ti-34Al-1B)			
	900/1 h/AC	1200/5 h/AC + 900/5 h/AC	
25°C YS [MPa (ksi)]	–	–	
UTS [MPa (ksi)]	392 (56.8)	221 (32.0)	
% Elongation	–	–	
Modulus [GPa (Msi)]	112 (16.3 Msi)	141 (20.4 Msi)	
815°C YS [MPa (ksi)]	–	–	
UTS [MPa (ksi)]	101 (14.7)	139 (20.2)	
% Elongation	–	–	
900°C YS [MPa (ksi)]	–	–	
UTS [MPa (ksi)]	93 (13.5)	97 (14.1)	
% Elongation	–	–	
Alloy 6 (Ti-34Al-2Er)			
25°C YS [MPa (ksi)]	–	–	
UTS [MPa (ksi)]	480 (69.7)	290 (42.0)	
% Elongation	0.1	–	
Modulus [GPa (Msi)]	150 (21.8 ksi)	149 (21.6)	
815°C YS [MPa (ksi)]		–	
UTS [MPa (ksi)]		419 (60.8)	
% Elongation		–	
900°C YS [MPa (ksi)]		–	
UTS [MPa (ksi)]		538 (78.0)	
% Elongation		0.1	

90-224-175c

strength but comparable elevated-temperature strengths, as shown in Figure 43.

The Er additions to the Ti-2Er alloy (alloy 2) resulted in lower strength, but better ductility than alloy 1. These values are comparable to those of the EBSQ Ti-2Er flakes reported earlier. The 1000°C/5 h/AC heat treatment, which resulted in coarser particles and a coarser microstructure than the 800°C/1 h/AC treatment, produced reduced strength values at 25 and 500°C. However, the 800°C/24 h/AC treatment, which resulted in the coarsest particles in a microstructure containing grain boundary α, produced the best strength/ductility combination. The flow stress as a function of temperature for alloy 2 is shown in Figure 44.

Whereas the Ti-2Er alloy has significantly higher strength at 25°C than the Ti-1B alloy, Ti-1B retains its strength better at elevated temperatures, as shown in Figure 45.

The Ti-16Al-1B alloy (alloy 3), which contains extremely large borides (~6 μm mean length), lacked ductility at 25°C. However its modulus (150 GPa) was considerably higher than that of conventional titanium alloys (~110 GPa). The 850°C/1 h/AC heat treatment, which yielded slightly longer and thinner borides, produced slight ductility at 600°C and good ductility at 815°C. The strength value of 425 MPa at 815°C compares very favorably to those of γ-based titanium aluminides, viz. 475 MPa for Ti-34Al (Reference 13).

The Ti-16Al-2Er alloy (alloy 4) is quite similar to the Ti-16Al-1B alloy since ductility is lost at 25°C, and the alloy has high strength and marginal ductility at elevated temperatures. In contrast to the coarse borides of alloy 3, the Er_2O_3 particles in alloy 4 are quite fine (~1 - 2 μm diameter). The interstitial levels in these two alloys (0 + C = 0.23 wt%) are considerably lower than in alloys 1 and 2, but nevertheless are probably limiting the ductility of these alloys.

Ti-34Al-1B (alloy 5) did not exhibit any ductility at either room or elevated temperatures. This severe brittleness is most likely a consequence of the high interstitial content (0 + C = 0.41 wt%) in this alloy.

The Ti-34Al-2Er alloy (alloy 6) did not exhibit any ductility after the 1200°C/5 h/AC + 900°C/5 h/AC anneal. It had very slight ductility (~0.1%)

90-224-170c

Figure 43. Yield stress as a function of temperature for Ti-1B after (o) 800°C/1 h/AC, (□) 800°C/24 h/AC, and (◊) 1,000°C/5 h/AC; and (△) unalloyed titanium.

90-224-171c

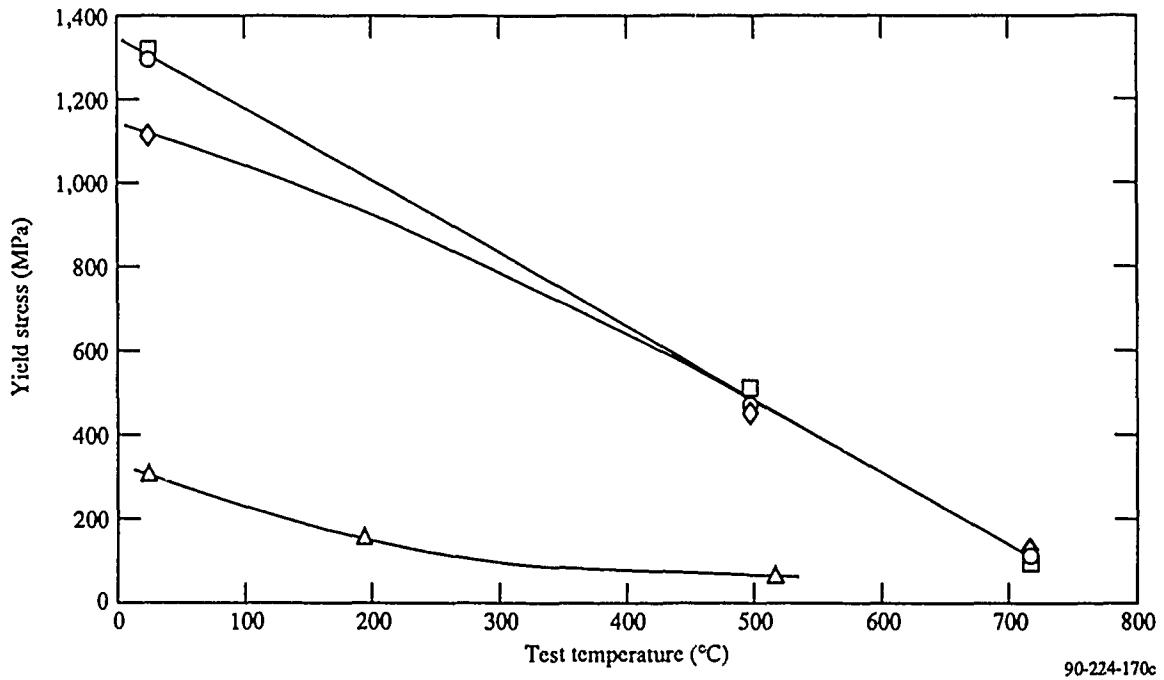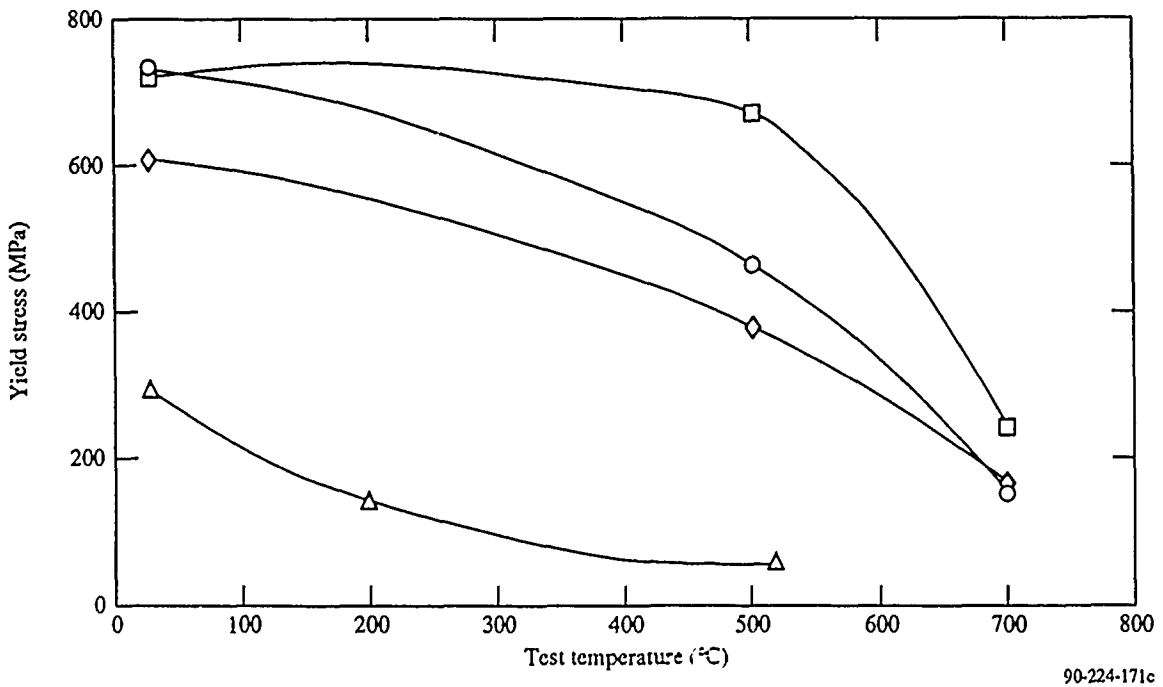Figure 44. Yield stress as a function of temperature for Ti-2Er after (o) 800°C/1 h/AC, (□) 800°C/24 h/AC, and (◊) 1,000°C/5 h/AC; and (△) unalloyed titanium.
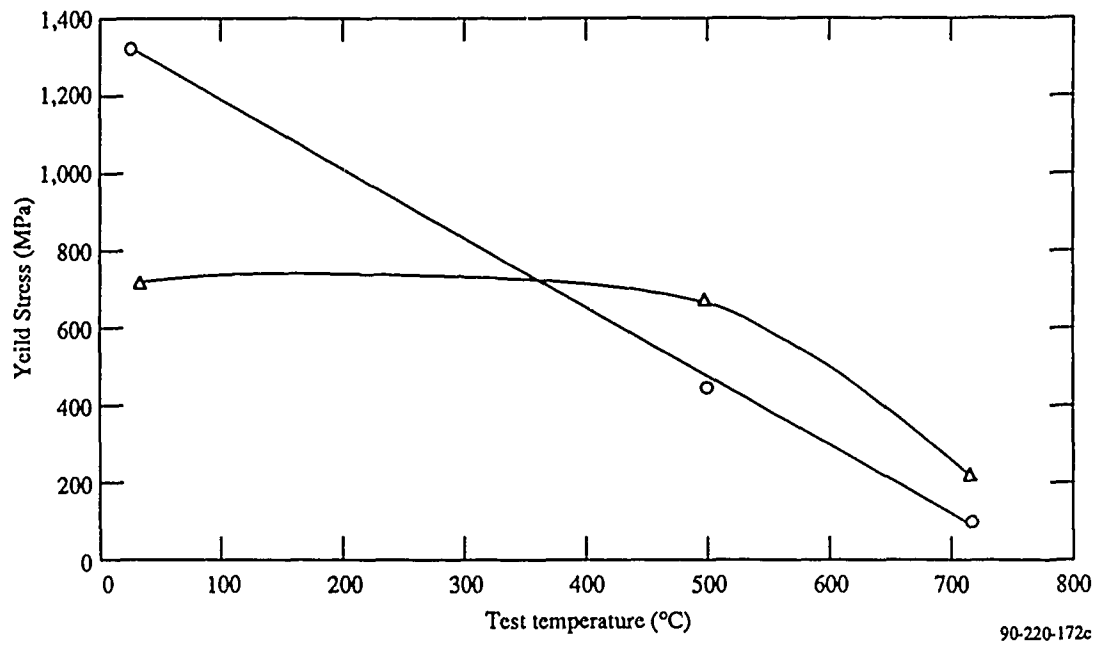
Figure 45. Yield stress as a function of temperature for (○) Ti-1B after 800°C/24 h/AC and
(△) Ti-2Er after 800°C/24 h/AC.

90-220-172c

at 25°C after the 900°C/1 h/AC heat treatment, but no increase in strength over Ti-34Al (Reference 13).

6. SUMMARY AND CONCLUSIONS

Large volume fractions of uniformly distributed strengthening reinforcements were produced in rapidly solidified α-Ti, Ti_3Al (α_2), and TiAl (γ) alloys with boron and erbium additions.

In rapidly solidified α Ti-B, and Ti_3Al-B alloys, in agreement with reported phase diagram for Ti-B, titanium monoborides (TiB) with rod-like and needle-like morphology and the long axes of the needles ($[010]_{TiB}$) parallel to the close-packed directions on the basal planes of α Ti and Ti_3Al are formed by solid state precipitation during cooling. Rapid solidification of TiAl-B alloys, however, results in the formation of titanium diboride (TiB_2) with blocky morphology. The differences in boride morphologies are related to matrix crystal structures and the stages of solidification process during which they evolve (Reference 14). In TiB, the (100) and ($10\overline{1}$) planes have higher packing densities than (101) and (001) planes respectively. Growth along [100] involves alternate B and Ti planes, whereas growth along [001] involves planes of equiatomic stoichiometry. Thus, the (001) planes are likely to exhibit fastest growth, leaving the crystal bound by (100) and {101} type facets. In the case of TiB_2, the trigonal prisms are closely packed in all directions with growth along the [0001] and $\langle 1100 \rangle$ directions involving alternating Ti and B layers in both cases. Thus the primary crystals growing from the melt tend to have fairly equiaxed shapes. The observed TiB and TiB_2 morphologies are in agreement with the above crystallographic considerations.

The dispersoids in Er containing α Ti and γ TiAl were identified as Er_2O_3. The Er_2O_3 dispersoids are incoherent with the matrix and exhibit spherical morphology in α Ti. In γ TiAl, however, during early stages of dispersoid formation, the Er_2O_3 dispersoids are coherent with the matrix, and exhibit faceted morphology with cubic orientation relationships, i.e., $(100)\gamma || (100)Er_2O_3$, $(010)\gamma || (010)Er_2O_3$, and $(001)\gamma || (001)Er_2O_3$.

The interface boundaries in two phase γ + α_2 alloys were systematically characterized and six distinct types of boundaries were identified. These

boundaries markedly influence the slip transmittal across the γ/α_2 interfaces and therefore provide an additional degree of freedom for optimizing the mechanical properties of γ-based alloys.

The boride and erbium oxide dispersoids produce large strength and modulus increases and significant ductility decrease in all the alloys.

7. PUBLICATIONS RESULTING FROM THIS CONTRACT

1. S. M. L. Sastry, "Microstructure Control of Titanium Alloys by Rapid Solidification Processing," presented at the Workshop on Advanced Processing of Intermetallics and Intermetallic Composites, University of California, Santa Barbara, CA, 5-16 January 1987.

2. S. M. L. Sastry, "Effects of Reinforcements on Creep and Fracture Toughness of Titanium Alloys," DARPA Materials Research Council Meeting, La Jolla, CA, 6-10 July 1987.

3. D. S. Schwartz, "Twin and Fault Structures in Titanium Aluminide," 1988 Aluminides Meeting, Stratford, CT, November 1988.

4. S. M. L. Sastry, "Fatigue and Fracture of Gamma TiA1," 1988 Aluminides Meeting, Stratford, CT, November 1988.

5. D. S. Schwartz and S. M. L. Sastry, "Twin and Fault Structures in Titanium Aluminides," Scr. Metall. 23, 1621-1626 (1989).

6. D. S. Schwartz and S. M. L. Sastry, "Structural Analysis of Special Grain Boundaries in Ti-36Al," presented at the Annual TMS/ASM fall meeting, Indianapolis, IN, 2 October 1989.

7. S. M. L. Sastry, "Titanium Aluminides: A Review of Current Status," presented at the 2nd Workshop on Hydrogen-Materials Interactions, Scottsdale, AZ, 1-3 June 1988.

8. S. M. L. Sastry, "Improvement of Titanium Alloy Microstructures and Properties by Rapid Solidification Processing," in Rapid Solidification Processing Principles and Techniques IV, R. Mehrabian and P. A. Parrish, eds. (Claitor's Publishing, Baton Rouge, LA, 1988), p. 165.

9. D. S. Schwartz and S. M. L. Sastry, "Microstructure of Borides in Titanium and Titanium Aluminides," submitted to Proceedings of the XII International Congress for Electron Microscopy, 1990, Seattle, WA.

10. D. S. Schwartz, P. Fraundorf, and S. M. L. Sastry, "High-Resolution TEM of B- and Er-Containing Precipitates," submitted to Conference Proceedings of Frontiers of Electron Microscopy in Materials Science, 1990.

8. COUPLING ACTIVITIES WITH GROUPS PERFORMING RELATED RESEARCH

1. Presentations on MDRL/AFOSR research on Ti and Nb were made to Mr. Dan Miracle, Mr. Dennis Dimiduk, Mr. Siameck Mazdiazni, and Mr. Bill Kerr (AFWAL/LLM) June 1987.

2. Discussions were held during the TMS/AIME Fall Meeting, Cincinnati, 11-15 October 1987 with Prof. Henry Rack of Clemson University on high-temperature deformation of RST Ti and Nb in situ composites, with Bruce MacDonald of National Science Foundation on RST Ti and Nb microstructures, and with Prof. Rama Ankem of University of Maryland on modeling of deformation of in situ composites.

3. Discussions were held in January 1987 with Professors J. Perepezko and R. Mehrabian on rapidly solidified microstructures, and with Professors A. G. Evans and B. Budianski on toughening effects of high-modulus reinforcements in TI alloy matrices.

4. Discussions were held in 1987 with Prof. A. K. Mukherjee, University of California-Davis, on dispersion strengthening of niobium alloys.

5. Discussions were held in 1988 and 1989 with Dr. A. Giamei, United Technologies Research Center, on microstructures of rapidly solidified Ti and Nb alloys.

6. Discussions were held in 1988 and 1989 with Prof. P. Fraundorf, Dept. of Physics, University of Missouri, St. Louis, on high-resolution microscopic studies of fine structure of titanium aluminides.

9. REFERENCES

1. S. M. L. Sastry, P. J. Meschter, and J. E. O'Neal, "Structure and Properties of Rapidly Solidified Dispersion Strengthened Titanium Alloys, Part I: Characterization of Dispersoid Distribution, Structure, and Chemistry," Metall. Trans. 15, 1451 (1984).

2. S. M. L. Sastry, T. C. Peng, and J. E. O'Neal, "Design and Development of Advanced Titanium Alloys by Rapid Solidification," in Titanium Science and Technology, G. Lutjering, U. Zwicker, and W. Bunk, eds. (Deutsche Gesellschaft für Metallkunde, E.V., FRG, 1985), p. 397.

3. J. H. Perepezko and W. J. Boettinger, Proc. Materials Research Society Symposium on Alloy Phase Diagrams (Elsevier-North Holland, 1983), pp. 223-229.

4. T. C. Peng, S. M. L. Sastry, and J. E. O'Neal, "Rapid Solidification Processing of Titanium Alloys," in Titanium Science and Technology, G. Lutjering, U. Zwicker, and W. Bunk, eds. (Deutsche Gesellschaft für Metallkunde, E.V., FRG, 1985), p. 389.

5. M. J. Blackburn, in The Science, Technology and Application of Titanium, R. Jaffee and N. Promisel, eds. (Pergamon Press, Oxford, 1970), p. 633.

6. D. Shechtman, M. J. Blackburn, and H. A. Lipsitt, Metall. Trans. 5, 1373 (1974).

7. D. W. Pashley, J. L. Robertson, and M. J. Stowell, Phil. Mag. 19, 83 (1969).

8. J. W. Christian and D. E. Laughlin, Acta Metall. 36, 1617 (1988).

9. C. R. Feng, D. J. Michel, and C. R. Crowe, Scr. Metall. 22, 1481 (1988).

10. B. Aaronson et al., in Borides, Silicides and Phosiphides (John Wiley, New York, 1965), pp. 47-56.

11. H. R. Odgen et al., "Structure and Properties of Ti-C Alloys," Trans. TMS-AIME, 203, 73-80 (1955).

12. R. A. Wood and R. J. Favor, in Titanium Alloys Handbook (Battelle Columbus Laboratories, MCIC-HB-02, 1985), pp. 5-1:72.4-72.8.

13. S. M. L. Sastry, W. O. Soboyejo, and R. J. Lederich, "Hydrogen Effects in Gamma Titanium Aluminides," 3rd NASP Workshop on Hydrogen-Materials Interactions, Scottsdale, AZ, 31 May - 2 June 1989.

14. M. E. Hyman, C. McCullough, J. J. Valencia, C. G. Levi, and
    R. Mehrabian, "Microstructure Evolution in TiAl Alloys with B Additions:
    Conventional Solidification," University of California-Santa Barbara,
    Santa Barbara, CA, July 1988.